Cell Reports

Article

Modular basis for potent SARS-CoV-2 neutralization by a prevalent VH1-2-derived antibody class

Graphical abstract

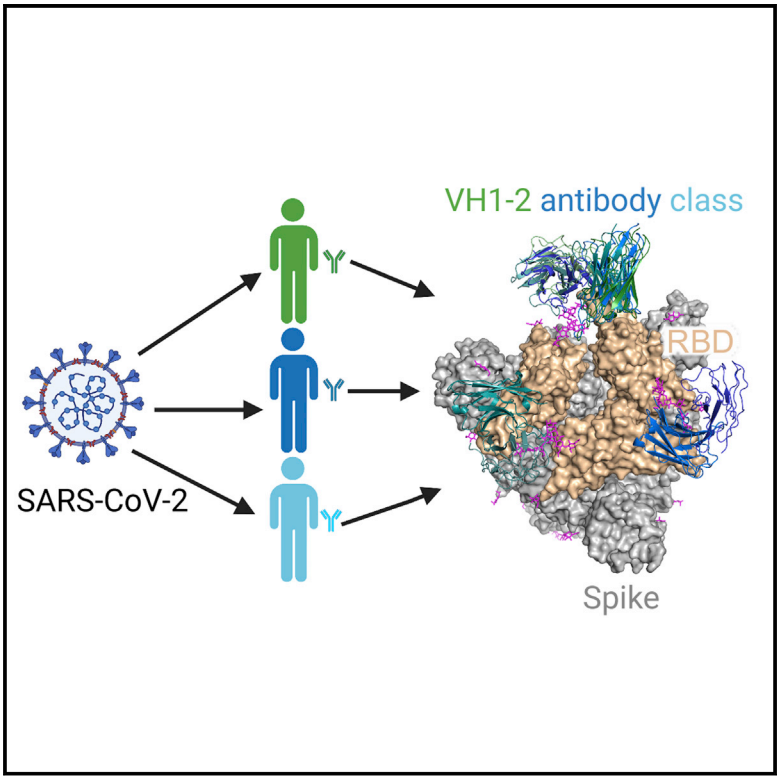

Authors

Micah Rapp, Yicheng Guo, Eswar R. Reddem, ..., David D. Ho, Lawrence Shapiro, Zizhang Sheng

Correspondence

lss8@columbia.edu (L.S.), zs2248@cumc.columbia.edu (Z.S.)

In brief

Rapp et al. determine structures of three human VH1-2-derived SARS-CoV-2-neutralizing antibodies and define a prevalent multi-donor antibody class that recognizes the receptor-binding domain (RBD) with convergent heavy- and light-chain modules. They further show the structural basis for RBD-up and RBD-down recognition and quaternary recognition-mediated spike-conformation change.

Highlights

- Determine structures of SARS-CoV-2-neutralizing antibodies 2-43, 2-15, and H4
- Define a multi-donor VH1-2 antibody class for RBD and quaternary recognition
- Reveal structural basis of RBD-up and RBD-down recognition within the class
- Delineate changes in spike conformation induced by quaternary recognition

Rapp et al., 2021, Cell Reports *35*, 108950
April 6, 2021
https://doi.org/10.1016/j.celrep.2021.108950

CellPress

Cell Reports

CellPress
OPEN ACCESS

Article

Modular basis for potent SARS-CoV-2 neutralization by a prevalent VH1-2-derived antibody class

Micah Rapp,[1,2,5] Yicheng Guo,[1,2,3,5] Eswar R. Reddem,[1,2,5] Jian Yu,[3,5] Lihong Liu,[3] Pengfei Wang,[3] Gabriele Cerutti,[1,2] Phinikoula Katsamba,[2] Jude S. Bimela,[2] Fabiana A. Bahna,[2] Seetha M. Mannepalli,[2] Baoshan Zhang,[4] Peter D. Kwong,[1,4] Yaoxing Huang,[3] David D. Ho,[3] Lawrence Shapiro,[1,2,3,4,*] and Zizhang Sheng[2,3,6,*]

[1]Department of Biochemistry and Molecular Biophysics, Columbia University, New York, NY 10032, USA
[2]Zuckerman Mind Brain Behavior Institute, Columbia University, New York, NY 10027, USA
[3]Aaron Diamond AIDS Research Center, Columbia University Vagelos College of Physicians and Surgeons, New York, NY 10032, USA
[4]Vaccine Research Center, National Institute of Allergy and Infectious Diseases, National Institutes of Health, Bethesda, MD 20892, USA
[5]These authors contributed equally
[6]Lead contact
*Correspondence: lss8@columbia.edu (L.S.), zs2248@cumc.columbia.edu (Z.S.)
https://doi.org/10.1016/j.celrep.2021.108950

SUMMARY

Antibodies with heavy chains that derive from the VH1-2 gene constitute some of the most potent severe acute respiratory syndrome coronavirus 2 (SARS-CoV-2)-neutralizing antibodies yet identified. To provide insight into whether these genetic similarities inform common modes of recognition, we determine the structures of the SARS-CoV-2 spike in complex with three VH1-2-derived antibodies: 2-15, 2-43, and H4. All three use VH1-2-encoded motifs to recognize the receptor-binding domain (RBD), with heavy-chain N53I-enhancing binding and light-chain tyrosines recognizing F486$_{RBD}$. Despite these similarities, class members bind both RBD-up and -down conformations of the spike, with a subset of antibodies using elongated CDRH3s to recognize glycan *N*343 on a neighboring RBD—a quaternary interaction accommodated by an increase in RBD separation of up to 12 Å. The VH1-2 antibody class, thus, uses modular recognition encoded by modular genetic elements to effect potent neutralization, with the VH-gene component specifying recognition of RBD and the CDRH3 component specifying quaternary interactions.

INTRODUCTION

Studies on human antibody responses to viral pathogens, including HIV-1, influenza, Ebola, and malaria, have revealed prominent classes of similar neutralizing antibodies (nAbs), which arise commonly in numerous individuals in response to infection or vaccination (Ehrhardt et al., 2019; Imkeller et al., 2018; Joyce et al., 2016; Kallewaard et al., 2016; Pappas et al., 2014; Zhou et al., 2013, 2015). Such multi-donor antibody classes are defined based on similar V(D)J gene recombination and similar modes of structural recognition—with this combination indicative of a common evolutionary process in antibody development (Kwong and Mascola, 2012). Multi-donor antibody classes are thought to arise based on effective function, combined with genetic accessibility because of class requirements for V(D)J recombination and somatic hypermutations of sufficient frequency to be present in the antibody human repertoire. Some multi-donor antibody classes are potent, broadly neutralizing, and frequent in human antibody repertoire (Imkeller et al., 2018; Joyce et al., 2016; Zhou et al., 2013). A prominent mode of rational vaccine design, ''lineage-based vaccine design,'' endeavors to elicit such antibody classes by vaccination (Haynes et al., 2012; Jardine et al., 2013; Kwong and Mascola, 2018), and this approach to human vaccination has recently entered clinical assessment (Diemert and McElrath, 2018).

Severe acute respiratory syndrome coronavirus 2 (SARS-CoV-2), the causative agent of the ongoing coronavirus disease 2019 (COVID-19) pandemic, has infected more than 80 million people and has claimed over 1 million deaths since the outbreak began in late 2019 (Dong et al., 2020; Zhou et al., 2020; Zhu et al., 2020). Therapies and vaccines are urgently needed to end the pandemic. Many nAbs have now been isolated from COVID-19 convalescent donors, with the most potent nAbs showing promise as prophylactic or therapeutic agents (Brouwer et al., 2020; Chen et al., 2020; Kreer et al., 2020; Liu et al., 2020a; Robbiani et al., 2020; Rogers et al., 2020; Tortorici et al., 2020; Zost et al., 2020). This growing set of nAbs provides an opportunity to identify effective human antibody responses to SARS-CoV-2 common in the population, which will inform therapeutic strategies and help to interpret vaccine readouts.

SARS-CoV-2 nAbs predominantly target the viral spike glycoprotein, which interacts with angiotensin-converting enzyme 2 (ACE2) receptors on the host-cell surface to mediate virus entry (Hoffmann et al., 2020; Wang et al., 2020). The ectodomain of the

prefusion spike comprises three copies of both S1 and S2 subunits (Wrapp et al., 2020). The S1 subunit is responsible for ACE2 binding, and the S2 subunit mediates fusion with host-cell membrane. Each S1 subunit comprises an N-terminal domain (NTD) and a receptor-binding domain (RBD). The RBDs are very flexible, adopting either an "up" conformation (open state) or a "down" conformation (closed state), with only the up RBDs capable of interacting with ACE2 (Wang et al., 2020). Currently, many nAbs have been characterized that bind to epitopes on either the up and/or down RBDs (Barnes et al., 2020a; Liu et al., 2020a; Tortorici et al., 2020). These RBD-targeting nAbs neutralize SARS-CoV-2 through mechanisms that include competition with ACE2 for RBD binding and locking the RBDs in the down conformation.

Human SARS-CoV-2 nAbs develop with few somatic hypermutations and strong avidity effects (Barnes et al., 2020b; Kreer et al., 2020; Liu et al., 2020a; Robbiani et al., 2020). Characterization of genetic features of SARS-CoV-2 nAbs identified to date show enrichment of antibody-variable genes, including VH3-53, VH1-2, VH1-69, VH3-66, VH1-58, and VH3-30 (Liu et al., 2020a; Robbiani et al., 2020; Yuan et al., 2020). So far, structural characterization of multiple nAbs have revealed two separate RBD-targeted classes derived from the similar VH3-53 and VH3-66 genes. One of these is characterized by heavy-chain complementarity-determining region 3 (CDRH3) of 15 amino acids or shorter—and recognizes the RBD ridge in the up position on SARS-CoV-2 spike (type I) (Yuan et al., 2020). The second VH3-53/-66 class—with longer CDRH3s—recognizes a similar region of RBD but adopts an approach angle with the heavy- and light-chain orientation rotated 180° (type II), suggesting CDRH3 to be critical for the classification of VH3-53/-66 antibodies (Barnes et al., 2020a; Wu et al., 2020a). Different VH3-30 originated antibodies can recognize at least three different regions of RBDs (Barnes et al., 2020a; Hansen et al., 2020), demonstrating that they do not form a single gene-restricted antibody class. Nevertheless, whether nAbs derived from VH1-2 and other germline genes form gene-restricted classes that represent shared effective antibody responses remains unaddressed. Currently, three VH1-2, potent nAbs (2-4, S2M11, and C121) show similar modes of RBD recognition but differences in quaternary epitope recognition (Barnes et al., 2020a; Liu et al., 2020a; Tortorici et al., 2020). It is, thus, still unclear whether RBD-targeting VH1-2 antibodies form a gene-restricted class. If so, what are the key genetic and structural signatures and determinants of neutralization potency?

Here, we present the structures of three VH1-2-derived nAbs (2-15, 2-43, and H4), revealing that they recognize a SARS-CoV-2 RBD epitope with similar modes of RBD recognition and similar angles of approach. Overall, recognition is modular with RBD predominantly recognized by a VH1-2-gene-encoded module. The second recognition module is represented by the diverse CDRH3s of the VH1-2 antibodies, which mediate quaternary recognition of N343 glycan from an adjacent RBD for a subset of class members. Thus, we define a multi-donor VH1-2 antibody class; members of which can achieve very high neutralization potency, which is prevalent in human responses to SARS-CoV-2. The shared genetic and structural signatures inform strategies to improve members of the VH1-2 antibody class.

RESULTS

VH1-2 antibodies are prevalent in human response to SARS-CoV-2 infection

To identify common features of the human antibody response to SARS-CoV-2, 158 spike-specific antibodies with characterized neutralization potencies were collected from 10 studies (Table S1) (Brouwer et al., 2020; Hansen et al., 2020; Ju et al., 2020; Kreer et al., 2020; Liu et al., 2020a; Robbiani et al., 2020; Rogers et al., 2020; Tortorici et al., 2020; Wu et al., 2020b; Zost et al., 2020). The V(D)J gene usage analysis showed that VH1-2 was the second most frequently used germline gene (Figure 1A; 25 in total). Comparison of neutralization potencies revealed that 11 of 25 (44%) of the VH1-2 antibodies are potent (half maximal inhibitory concentration [IC_{50}] < 0.1 μg/mL; Figure 1B). Within four studies (Hansen et al., 2020; Liu et al., 2020a; Tortorici et al., 2020; Zost et al., 2020), VH1-2 antibodies ranked the most potent of gene-delimited sets of antibodies (IC_{50} ranges from 0.015 to 0.0007 μg/mL). All 25 of the VH1-2-derived antibodies have been reported to bind to the SARS-CoV-2 RBD (Brouwer et al., 2020; Hansen et al., 2020; Ju et al., 2020; Kreer et al., 2020; Liu et al., 2020a; Robbiani et al., 2020; Rogers et al., 2020; Tortorici et al., 2020; Wu et al., 2020b; Zost et al., 2020). Sequence alignment of the VH1-2 nAbs showed the heavy chains to carry few somatic hypermutations, with each having a unique CDRH3 with length varying from 11 to 21 amino acids (Figures 1C and S1A; Kabat definition), and using different D genes (Figure S1B). The VH1-2 antibodies used both kappa and lambda genes with enrichment of the IGLV2-14 gene (Figure 1C).

As described below, we determined structures of three nAbs: 2-15, 2-43, and H4, with the highly potent antibodies 2-15 and 2-43 isolated from donor 2 of our previous study (Liu et al., 2020a), whereas H4 was from a different donor (Wu et al., 2020b). The 2-15, 2-43, and H4 nAbs neutralize authentic SARS-CoV-2 "live" virus with an IC_{50} of 0.0007, 0.003, and 0.896 μg/mL, respectively. These three antibodies derived from different heavy- and light-chain gene recombinations and, hence, three different B cell lineages (Figure S1B). Both 2-43 and 2-15 use the DH2-15*01 gene and have a long CDRH3 of 20 amino acids (Figure S1C), but they have different HJ gene origins (JH6*03 and JH3*02, respectively). The light chains of 2-43 and 2-15 were derived from recombination of a novel allele of the VL2-14 gene with JL3*02 and JL1*01, respectively (Figure S1D). H4 used DH2-2*01 and JH2*01 genes and had a CDRH3 of 17 amino acids (Wu et al., 2020b). The H4 light chain was derived from VK2-40*01 and JK4*01.

Structures of antibodies 2-15, 2-43, and H4 in complex with SARS-CoV-2 spike or RBD

To understand SARS-CoV-2 spike recognition by the VH1-2-derived antibodies, we used single-particle cryo-electron microscopy (cryo-EM) to produce high-resolution 3D-reconstructions of antigen-binding fragments (Fabs) from 2-15, 2-43, and H4 in

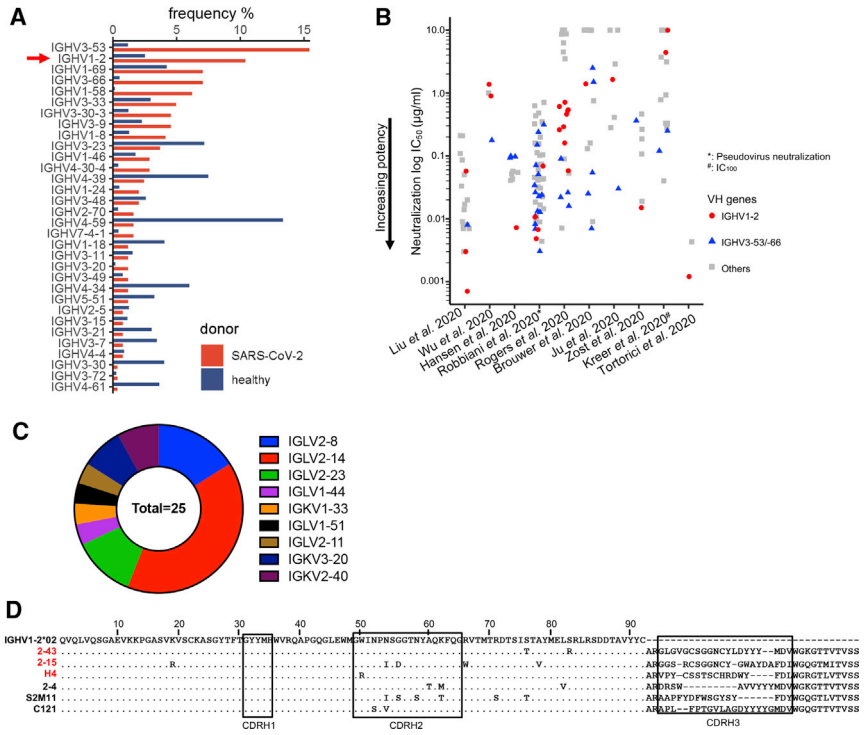

Figure 1. SARS-CoV-2 infection in humans induces potently neutralizing VH1-2 antibodies

(A) Gene usage of SARS-CoV-2-neutralizing antibodies. SARS-CoV-2 spike-specific VH1-2 antibodies are frequently induced in infected humans. VH1-2 antibodies are more-significantly enriched in the antigen-specific antibody repertoire than they are in healthy donors. Antibody repertoires from 17 healthy donors were used for the analysis.

(B) Many SARS-CoV-2-neutralizing VH1-2 antibodies (red) isolated from human donors achieve high potency, comparable with the most frequent IGHV3-53/-66 antibodies (blue). The half-maximal inhibitory concentration (IC_{50}) of neutralization is shown, except IC_{100} is shown for antibodies from Kreer et al., (2020). Live virus neutralization potency is shown for antibodies from nine studies, except the Hansen et al. (2020) study. IC_{50} values greater than 10 μg/mL are set to 10 μg/mL. Neutralizing antibodies targeting both RBD and non-RBD epitopes are included.

(C) SARS-CoV-2-neutralizing VH1-2 antibodies use diverse light-chain genes.

(D) Sequence alignment of the heavy chain of six VH1-2 antibodies. Antibodies with structures reported in this study are highlighted in red. Residues identical to germline gene are shown as dots.

See also Figure S1 and Table S1.

complex with the SARS-CoV-2 spike (Table S2). The reconstruction of the 2-43 complex with spike, refined to a global resolution of 3.60Å (Figures S2A–S2E), is significantly improved than in our previous study (5.8Å resolution) (Liu et al., 2020a). The reconstruction revealed a predominant class with three Fab molecules bound per spike trimer (Figure 2A). Each 2-43 Fab used the heavy-chain-variable domain to bind one primary RBD, with an orientation similar to the previously published antibody 2-4 (Liu et al., 2020a), with all RBDs in the down conformation (Figure 2A). The 2-43 heavy and light chains also recognize a quaternary epitope from the adjacent RBD. The three-dimensional (3D) classification revealed less-populated states with 1 and 2 Fabs bound, but in every case, the Fab was bound to a down RBD. This dependence upon the down conformation is likely due to extensive interactions between the Fab CDRH3 loop and the N-linked glycosylation at residue N343 on the adjacent RBD (Figure S2E). This suggests a neutralization mechanism by which the Fab simultaneously occludes ACE2 binding and locks the RBDs in the down conformation.

For the complex of 2-15 with spike (Figure 2B), approximately 56% of the particles were bound to an RBD in the up conformation, and 44% bound to RBD in the down conformation (Figures S2F–S2I), differing from antibody 2-43, which bound only to down RBDs. Because of increased conformational heterogeneity of the RBD-up class, the RBD-down class was the focus of our structural analysis (Figure 2B). In our initial attempt, a 9-fold molar excess of Fab was incubated with the S trimer. However, this resulted in spike disassembly (Figure S2J). To overcome this issue for structural determination, we found that a 1:1 molar ratio left spike-complexes intact, although some spike disassembly was still observed (Figure S2K). Although we were unable to resolve the 2-15-to-spike interaction at an atomic resolution, the cryo-EM analysis did reveal the overall orientation of the Fab, along with the position of the peptide backbone for several of the CDR loops.

To understand the binding mode of the 2-15 at an atomic resolution, we determined the crystal structure of the 2-15 in complex with isolated RBD. The structure was determined by molecular replacement at 3.18-Å resolution to a final crystallographic R_{work}/R_{free} of 18.6%/23.8% with good overall geometry (Table S3). The electron density for RBD (corresponding to S1-subunit residues 333–527) was well defined for residues 344–518, with missing internal stretches of four (362–366) and seven (383–390) residues, with the C-terminal 18 residues (519–537) disordered (Figure 2C). For Fab 2-15, all residues were visualized in density, with the exception of heavy-chain residues 142–145 in the Fc region. We then docked the crystal structure to the 2-15-spike complex cryo-EM density map by superposing RBD from the crystal structure on RBD from the cryo-EM map, with subsequent rigid body fitting to density.

Overall, the conformation of the 2-15 in the crystal structure agrees with the density observed in the cryo-EM map of the complex with the spike—particularly in the V-gene-encoded CDR regions. However, the conformation of the long CDRH3 loop differs and is far more elongated in the crystal structure (Figure S2L). In the cryo-EM map, it appears that the CDRH3 loop is pushed away from the N343 glycan and the helix encompassing residues 364–371 from the adjacent down RBD. The two light chains exhibit more-significant conformational differences. Save for CDRL3, which bends slightly away from RBD in the

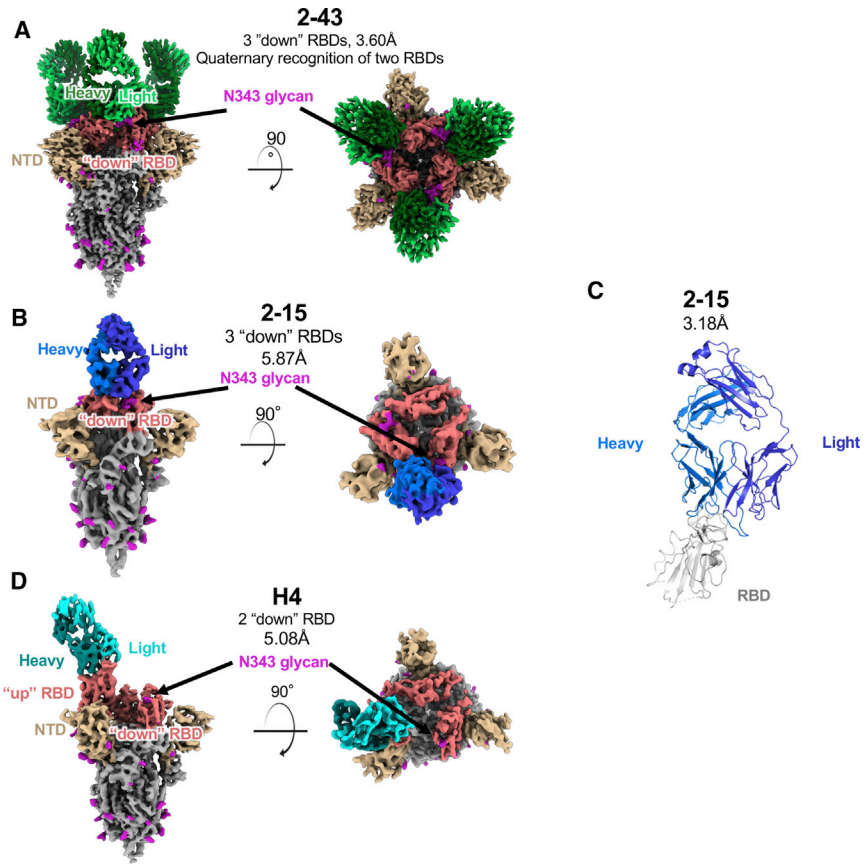

Figure 2. Structures of three SARS-CoV-2-neutralizing VH1-2 antibodies reveal both "RBD-down" and "RBD-up" modes of spike recognition

(A) Side and top views of three 2-43 antibody Fabs bound to the prefusion SARS-COV-2 spike in the closed state. Color schemes are 2-43, green; RBD, salmon; NTD, yellow; N-linked glycans, magenta; other spike regions, gray.

(B) Side and top views of one 2-15 antibody Fab in complex with the prefusion SARS-COV-2 spike in the closed state. 2-15 is colored blue.

(C) Overview of the crystal structure of 2-15 in complex with SARS-CoV-2 RBD. Residue segments missing in the structure are shown as dashed lines.

(D) Side and top views of one H4 Fab recognizing an up RBD on the prefusion SARS-COV-2 spike. H4 is colored cyan.

See also Figure S2 and Tables S2 and S3.

crystal structure, the conformations of the loops are quite similar, but the chain is shifted down closer to the RBD.

Finally, a reconstruction of Fab H4 revealed spike complexes with a single Fab bound to RBD in the up conformation (Figures 2D and S2M–S2P). Interestingly, no Fab was seen bound to a down RBD. The conformational flexibility of the RBD in the up conformation made a high-resolution cryo-EM reconstruction unattainable, and the map was refined to an overall resolution of 5.08 Å. Similar to Fab 2-15, the peptide backbone for many CDR loops was observed, and a homology model of the Fab variable domain was docked into the density. The superimposition of modeled H4 to the 2-43/spike complex showed that H4 adopts an RBD approaching angle similar to that of 2-43 (Figure S2Q). However, the light chain of H4 rotates toward the interface between RBDs such that the long CDRL1 of H4 clashes with N343 glycan from an adjacent down RBD (Figure S2R), which suggests a possible explanation for the apparent lack of H4 binding to down RBDs.

Conserved mode of RBD recognition

To understand the similarity in RBD recognition, we characterized the epitope and paratope interactions of 2-43 and 2-15 and compared them with the three published VH1-2 antibodies: 2-4, S2M11, and C121 (Barnes et al., 2020a; Liu et al., 2020a; Tortorici et al., 2020). Overall, 2-43 interacts predominantly with the receptor-binding motif (RBM; residues 438–508) on one down RBD protomer and simultaneously binds the N343 glycan from an adjacent down RBD protomer (Figure 3A). We describe the N343 glycan interaction below in the last section focused on quaternary interactions. The interaction between 2-43 and the "primary" RBD bound through its RBM buries a total of 756-Å^2 paratope body surface area (BSA); 83% of which is contributed by heavy chain (Figures 3A and S3A). Heavy-chain framework 1 (FWH1), CDRH1, CDRH2, and CDRL3 of 2-43 form hydrogen-bond networks with three RBD regions. In the first region, residues in FWH1 and the DE-loop in FWH3 form a groove to hold $Y449_{RBD}$. Hydrogen bonds are observed between FWH1 residues and $Y449_{RBD}$ and $Q498_{RBD}$ (Figure 3A, second panel). In the second region, involving the "flat" region of RBM, $T30_{HC}$ forms a hydrogen bond with $S494_{RBD}$. In the third region or the RBD ridge region, $Y33_{HC}$, $N52_{HC}$, and $S54_{HC}$ form a hydrogen-bond network with $E484_{RBD}$. Light-chain residues $Y91_{LC}$ and $S95_{LC}$ further the hydrogen bond with $G485_{RBD}$ and $F486_{RBD}$. In addition, $Y30_{LC}$, $Y32_{LC}$, $Y91_{LC}$, and $Y100j_{HC}$ also form a hydrophobic pocket to hold $F486_{RBD}$ (Figure S3B), with π-π stacking observed between $Y30_{LC}$ and $F486_{RBD}$ (Figure 3A, right panel).

The crystal structure of 2-15 complexed with SARS-CoV-2 RBD revealed 2-15 to use similar heavy- and light-chain regions to recognize the RBM (Figure 3B, left panel). Similar to 2-43, 2-15 forms convergent hydrogen bonds to $Y449_{RBD}$, $S494_{RBD}$, $E484_{RBD}$, and $G485_{RBD}$ as well as π-π stacking with $F486_{RBD}$ (Figure 3B, right three panels). Nonetheless, 2-15 interactions that are different from 2-43 are also observed at the RBM flat and ridge regions (Figure 3B, right two panels).

Compared with 2-43 and 2-15, the published VH1-2 antibodies, 2-4, S2M11, and C121, showed a similar RBM approach angle and binding mode (Figures 3C, 3D, S3C, and S3D). Typically, interactions between the VH1-2 antibodies and the RBD are mediated predominantly by the heavy chain (RBD_A column in

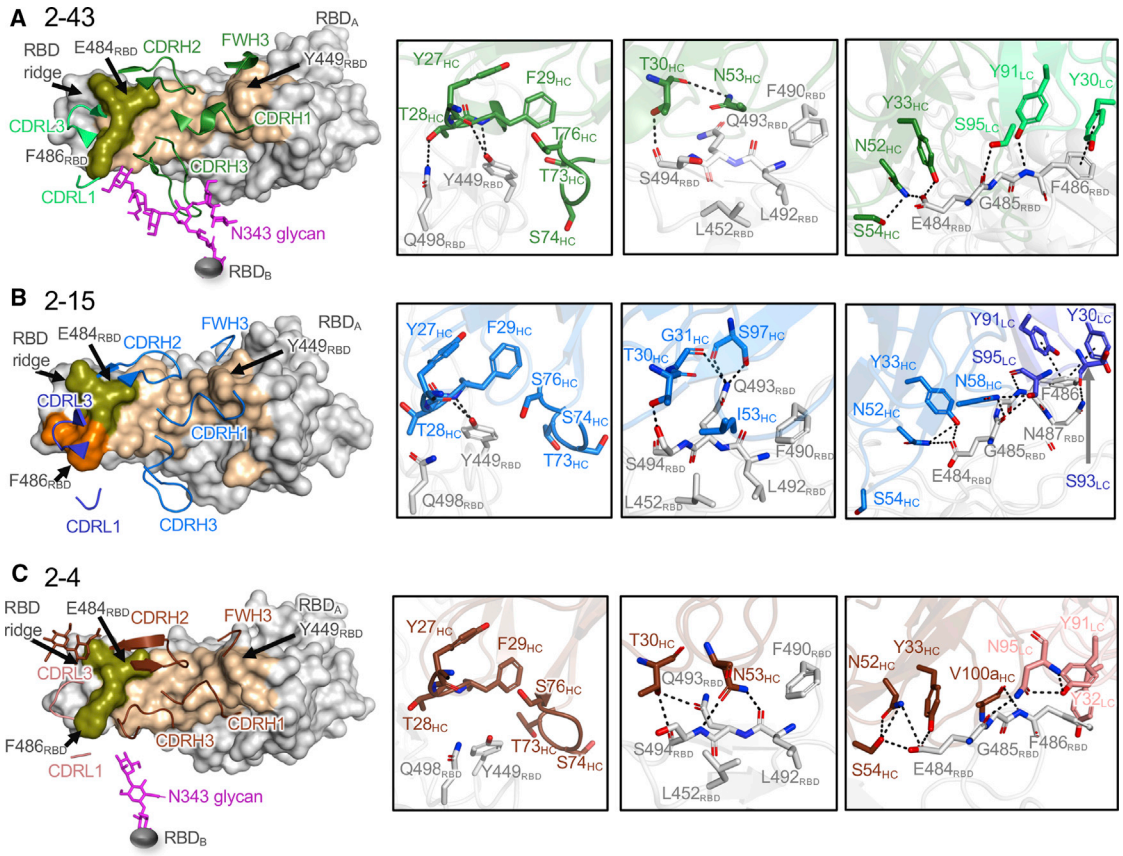

Figure 3. Common epitope-paratope interactions define a VH1-2 antibody class

(A) Overview of the 2-43 epitope (left panel) and close-up view of the hydrogen bond networks between 2-43 and the SARS-CoV-2 RBD (right three panels). The RBD epitope recognized by 2-43 heavy (forest) and light (lime green) chains are colored wheat and orange, respectively (RBD_A, light gray). Epitope residues interacting with both heavy and light chains are colored lemon. 2-43 also binds to the N343 glycan (magenta) from a neighboring RBD (RBD_B, dark gray). Hydrogen bonds and π-π stacking are shown as black dashed lines.

(B) Overview of the epitope of 2-15 (left panel) and close-up view of the hydrogen bond networks and π-π stacking between 2-15 and the SARS-CoV-2 RBD (right three panels). 2-15 heavy and light chains are colored marine and blue, respectively. Epitope residues interacting with both heavy and light chains are colored lemon.

(C) Overview of the epitope of 2-4 (left panel) and close-up view of the hydrogen-bond networks between 2-4 and the SARS-CoV-2 RBD (right three panels). The heavy and light chains of 2-4 are colored chocolate and salmon, respectively. Epitope residues interacting with both heavy and light chains are colored lemon. See also Figure S3.

Figure S3C). For all antibodies, the VH1-2-gene-encoded residues form a module for RBM recognition. Despite these antibodies having different light-chain gene origins, convergent tyrosine residues in CDRL1 and CDRL3 pack against $F486_{RBD}$ (Figure S3B), which constitutes another module for RBD recognition. Because each antibody has a unique CDRH3, no conserved polar or hydrophobic interaction is observed (Figures 3 and S3B–S3D), albeit CDRH3 contributes the most BSA among the CDRs, except in 2-15 (Figure S3A). Altogether, the germline gene residues from the VH1-2 gene as well as light-chain V genes anchor the antibodies to the RBM in a similar mode with the heavy-chain V region having a dominant role in determining the mode of recognition.

The VH1-2 antibody class and similarity to other SARS-CoV-2 RBD targeting antibodies

To gain an overall understanding of the similarity in the binding orientations of the VH1-2 antibodies, we superposed RBD and antibody complexes and calculated pairwise root-mean-square deviation (RMSD) to compare relative binding orientations of the six VH1-2 antibodies (2-43, 2-15, H4, 2-4, C121, and S2M11) as well as the 31 additional RBD-targeting antibodies originated from other VH genes. Overall, the VH1-2 antibodies have similar binding orientations (Figures 4A, 4B, and S4A). Their epitopes overlap with the ACE2 binding site (Figures S4B and S4C). The similarity in their genetic origin, details of their interactions with RBD (unavailable for H4), and their angles of approach, suggests that these six antibodies form a VH1-2 antibody class.

The structural, recombination, and somatic hypermutation analyses (described below in the next section) presented here revealed critical residues that determine the specificity and binding affinity of the VH1-2 class antibodies. We define residues forming the conserved side chain polar and/or hydrophobic interactions as genetic signatures. The heavy-chain signatures include a T30-x-x-Y33 motif in CDRH1 and an [NS]52-x-[NIV]-S54 motif

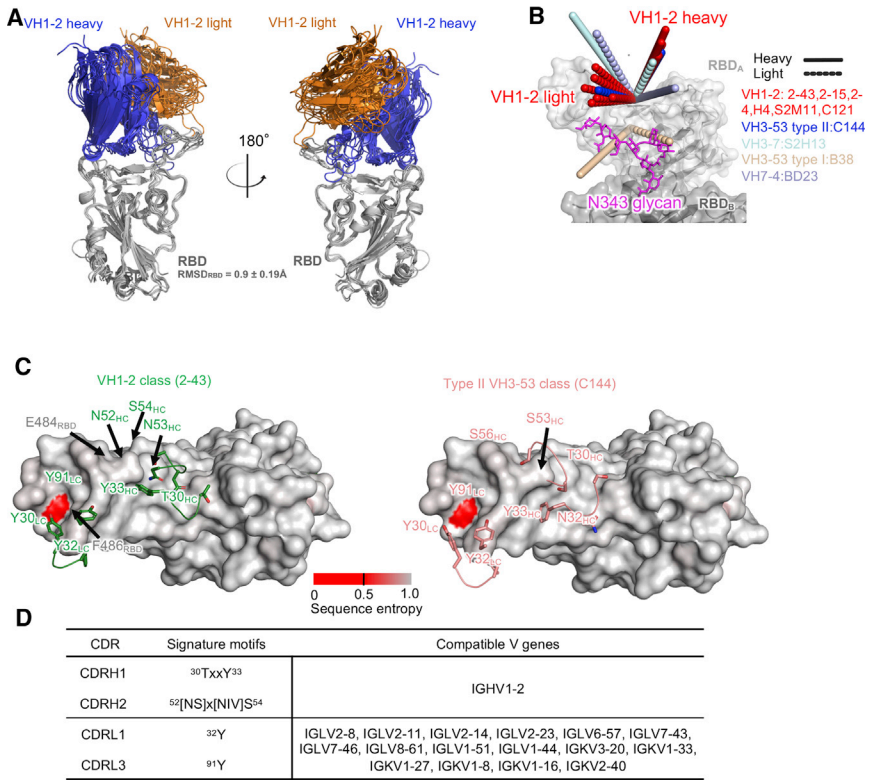

D

CDR	Signature motifs	Compatible V genes
CDRH1	^{30}TxxY^{33}	IGHV1-2
CDRH2	^{52}[NS]x[NIV]S^{54}	
CDRL1	^{32}Y	IGLV2-8, IGLV2-11, IGLV2-14, IGLV2-23, IGLV6-57, IGLV7-43, IGLV7-46, IGLV8-61, IGLV1-51, IGLV1-44, IGKV3-20, IGKV1-33, IGKV1-27, IGKV1-8, IGKV1-16, IGKV2-40
CDRL3	^{91}Y	

Figure 4. The VH1-2 antibody class

(A) Overview of modes of RBD recognition by the VH1-2 class antibodies: 2-43, 2-15, 2-4, H4, S2M11, and C121. The RBD and antibody complexes are superimposed on RBDs.

(B) Approach angles of SARS-CoV-2 RBD-targeting antibodies originated from different VH genes. Members of the VH1-2 antibody class have similar approach angles. The VH3-53 class antibody C144 has an angle of approach similar to that of the VH1-2 antibody class.

(C) Overview of VH1-2 signature motifs (green) and type II VH3-53 class (orange) on the RBD surface. The RBD is colored with the conservation score calculated from the circulating SARS-CoV-2 strains. The 2-43 structure is used to generate the conservation plot. Residues in gray have no mutation, whereas residues colored red have relatively high mutation frequency.

(D) Signature motifs and compatible germline V genes of the VH1-2 antibody class.

See also Figures S1 and S4.

(x represents any amino acid) in CDRH2 (Figure 4C), with no conserved motif observed in CDRH3 (Figure S1A). Searches of germline gene databases using this signature showed only alleles of the VH1-2 gene to match both motifs (Figure 4E), suggesting that the antibody class is likely to be restricted to VH1-2.

For light chain, residues $Y32_{LC}$ and $Y91_{LC}$ are signature residues that interact with both the primary RBD (Figures 3 and S3B) and the N343 glycan from adjacent RBDs (described below in the quaternary recognition section). However, because the light-chain interaction signatures can be found in many germline genes (Figures 4D and S4D), the VH1-2 antibody class may not be restricted with respect to light-chain origin gene.

To understand the conservation of the VH1-2 antibody epitope, we calculated the conservation score for each RBD residue and observed that the flat region is highly conserved in the natural SARS-CoV-2 reservoir. The four RBD residues critical for VH1-2 antibody recognition—$Y449_{RBD}$, $E484_{RBD}$, $F486_{RBD}$, and $Q493_{RBD}$—showed low mutation frequencies (approximately 0, 3, 7, and 7 per 10,000 sequences, respectively). Nonetheless, SARS-CoV-2 strains with mutations at the four positions are resistant to C121 and S2M11 of the VH1-2 antibody class (Barnes et al., 2020a; Tortorici et al., 2020).

In addition, the VH1-2 antibodies show high similarity in approach angle and epitope to antibody C144 (Figures 4C and S4A), a type-II VH3-53/-66 antibody. However, C144 uses different CDRH1 and CDRH2 motifs for interacting with the conserved residues in the flat region and ridge of RBD (e.g., the N32-Y33 and [T/S]54-G-G-[T/S]57 motifs in the VH3-53/-66 antibodies) (Figure 4C) (Barnes et al., 2020a; Wu et al., 2020a). The CDRH2 of C144 shifts toward the RBD ridge, perhaps because the CDRH2s of the VH3-53/-66 genes are one residue shorter than the VH1-2 gene. Nonetheless, both antibody classes use similar light-chain genes, including VL2-14 and VL2-23, which provide key Tyr residues that interact with $F486_{RBD}$.

Somatic hypermutations and avidity improve antibody potency

To understand the effects of somatic hypermutation (SHM) on binding affinity and neutralization potency, we reverted SHMs in the paratope regions of 2-43, 2-15, and 2-4 to their germline residues individually and in combination. The 2-43 only has one SHM in the paratope region, $S76T_{HC}$ (Figure S1A); the reversion of which reduces the immunoglobulin G (IgG)-apparent binding affinity and pseudovirus neutralization potency by about 6-fold and 5-fold, respectively (Figures 5A, 5B, and S4E). For 2-15, three paratope SHMs were observed: $N53I_{HC}$, $G55D_{HC}$, and $Y32F_{LC}$. The reversion of $N53I_{HC}$ and $Y32F_{LC}$ individually reduced binding affinity by 56-fold and 12-fold, respectively (Figure 5A), as well as neutralization potency by 217-fold and 42-fold, respectively (Figure 5B). The results suggested that the $N53I_{HC}$ and $F32Y_{HC}$ mutations are critical for the affinity maturation of 2-15. Structural analysis showed that the $N53I_{HC}$ mutation allows the Ile side chain to fit a hydrophobic pocket on RBD (Figures 3B and S5A). A convergent mutation is also observed in S2M11 ($N53I_{HC}$) and C121 ($N53V_{HC}$). We then introduced the $N53I_{HC}$ mutation to 2-43 and 2-4 and observed significant improvements of both binding affinity and neutralization potency (both IC_{50} and maximum potency) (Figure 5). These results suggested that mutation to a hydrophobic residue at 53_{HC} can be used to improve members of the VH1-2 antibody class. The

A

Antibody variants	ka (1/Ms)	kd (1/s)	K_D^{app} (nM)	Pseudovirus neutralization IC_{50} (μg/ml)
2-43	2.09(1)x10^6	0.216(1)x10^{-3}	1.034(4)	0.103
2-43 T76S$_{HC}$	9.8(9)x10^6	5.9(5)x10^{-2}	6.01(5)	0.474
2-43 N53I$_{HC}$	1.83(4)x10^6	4.7(1)x10^{-4}	0.259(8)	0.003
2-15	4.97(2)x10^6	1.37(2)x10^{-4}	0.0275(4)	0.001
2-15 I53N$_{HC}$	5.96(3)x10^6	9.15(5)x10^{-3}	1.536(3)	0.217
2-15 D55G$_{HC}$	6.21(2)x10^6	2.42(2)x10^{-4}	0.0389(4)	0.003
2-15 I53N$_{HC}$ D55G$_{HC}$	7.93(5)x10^6	7.89(5)x10^{-3}	0.995(2)	0.035
2-15 F32Y$_{LC}$	2.17(1)x10^6	7.25(4)x10^{-4}	0.334(2)	0.042
2-15 I53N$_{HC}$ D55G$_{HC}$ F32Y$_{LC}$	3.2(4)x10^5	8.9(8)x10^{-3}	28(2)	0.894
2-4	1.470(6)x10^6	5.89(2)x10^{-4}	0.401(2)	0.132
2-4 T61A$_{HC}$	7.21(9)x10^6	1.85(3)x10^{-2}	2.57(1)	1.205
2-4 N53I$_{HC}$	1.473(3)x10^6	2.40(1)x10^{-4}	0.1626(8)	0.013

B

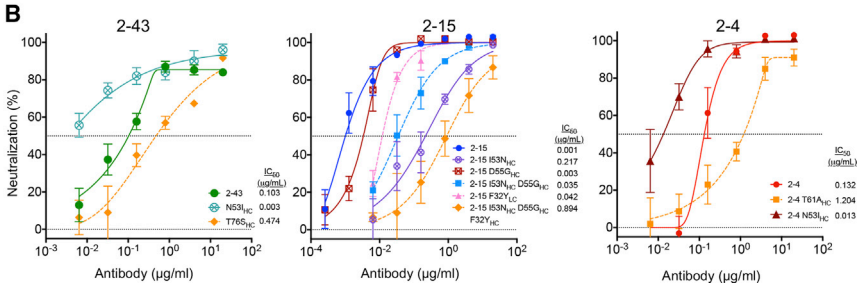

Figure 5. N53I mutation improves many VH1-2 class members

(A) Apparent binding affinities of 2-43, 2-15, and 2-4 IgGs and revertants. Somatic hypermutations improve the binding affinities of the three antibodies. N53I$_{HC}$ was introduced to 2-43 and 2-4 and showed a significantly increased binding affinity. The numbers in parentheses represent standard errors in the last integer.

(B) Pseudovirus neutralization profiles of 2-43, 2-15, 2-4, and their somatic hypermutation revertants. Data represent means ± SEM of technical triplicates.

See also Figures S1, S3, and S5.

crystal structure further showed that 2-15 32$_{LC}$ does not interact with RBD (Figure S3B); the Y32F$_{LC}$ SHM may alter the interaction with RBD indirectly. For 2-4, the SHM A60T$_{HC}$ generates an N-glycosylation site at position N58$_{HC}$. The N58$_{HC}$ glycan interacts with the RBD ridge (Figure 3C). The reversion of this SHM reduces binding affinity and neutralization by about 6-fold and 9-fold, respectively (Figure 5). In summary, somatic hypermutation analysis revealed that the precursors of these antibodies could bind antigens with nanomolar-apparent binding affinity, suggesting that the precursors of these antibodies can be activated efficiently by the SARS-CoV-2 spike protein. Nonetheless, SHMs significantly improve both the binding affinity and the neutralization potency of these antibodies. Because the observed SHMs are frequently generated by the somatic hypermutation machinery (Figure S1A), we anticipate that requirements for somatic hypermutations are unlikely to present a significant barrier for affinity maturation of this antibody class.

In addition, previous studies showed that bivalent binding (avidity) is critical for certain RBD-directed antibodies to achieve high potency (Barnes et al., 2020b; Liu et al., 2020b). We, therefore, examined whether avidity contributes to the observed high potency of the VH1-2 antibody class. Comparison of neutralization potency between IgGs and Fabs revealed that the Fabs of 2-43, 2-15, and 2-4 have potencies of about 140-, 95-, and 14-fold less than their IgG forms, respectively (Figure S5C), suggesting that avidity effects are critical for achieving high-neutralization potency by the VH1-2 class antibodies.

Recognition of quaternary epitopes modulates spike conformation

Our previous study with a low-resolution cryo-EM structure showed that 2-43 recognizes a quaternary epitope (Liu et al., 2020a). However, details on the quaternary interactions and their functional relevance have not yet been characterized. Here, high-resolution cryo-EM reconstructions revealed atomic-level interactions between 2-43 and the quaternary epitope. Overall, 2-43 interacts comprehensively with N343 glycan as well as helix 364–371 from an adjacent down-RBD protomer (RBD$_B$) (Figures 6A and S6A), burying a total of 999-Å BSA (Figure S3A). The quaternary interaction is predominantly mediated by the long CDRH3, which is held by the two branches of the N343 glycan; the structure of which is highly flexible and has not been observed in previous studies. The tip of one N343 glycan branch is further stabilized by hydrogen bonding with the 2-43 CDRL1 and the ridge of RBD$_A$ (Figure S6A). Altogether, 2-43 forms strong quaternary interactions with the adjacent down RBD, which is critical for locking RBDs in the all-down conformation. In contrast to 2-43, the cryo-EM density maps of the 2-15 and H4 spike complexes revealed no quaternary contacts (Figures 2D, S2L, and 6B).

Comparison of quaternary interactions among the five VH1-2-derived antibodies revealed two structural groups. Group 1 includes 2-43, 2-4, and S2M11, which bind predominantly down RBDs. Group 2 includes 2-15, H4, and C121, which bind both up and down or only up RBDs. For group 1, the quaternary recognition is mediated mostly by CDRH3, followed by CDRL1 and CDRL2 (Figures 6C and S3A). Differences between each antibody-specific CDRH3 determine that each antibody has a unique quaternary epitope (Figures 6A–C, S3B, and S6B). Different from other class members, which bind both the spike and isolated RBDs (Liu et al., 2020a; Robbiani et al., 2020; Tortorici et al., 2020; Wu et al., 2020b), the quaternary interaction is indispensable for 2-43 (Liu et al., 2020a). The quaternary epitope of 2-4, only part of which appears to be visible in the cryo-EM map (Liu et al., 2020a), comprises only the N343 glycan from the adjacent down-RBD protomer (Figure 6C), likely because 2-4 has a short CDRH3. The quaternary epitope of S2M11 includes the N343 glycan and helices 339–343 and 364–371 of the adjacent RBD (Figure S6B). Altogether, accommodation of the N343 glycan from the adjacent down RBD is a common feature of quaternary recognition by group-1 antibodies. The diverse CDRH3s of the group-1 antibodies form a module for quaternary recognition. In contrast, group-2 antibodies 2-15 and C121 show minor interactions with neighboring down RBDs (Figures 2C, 6B, S2R, and S3A), which may explain

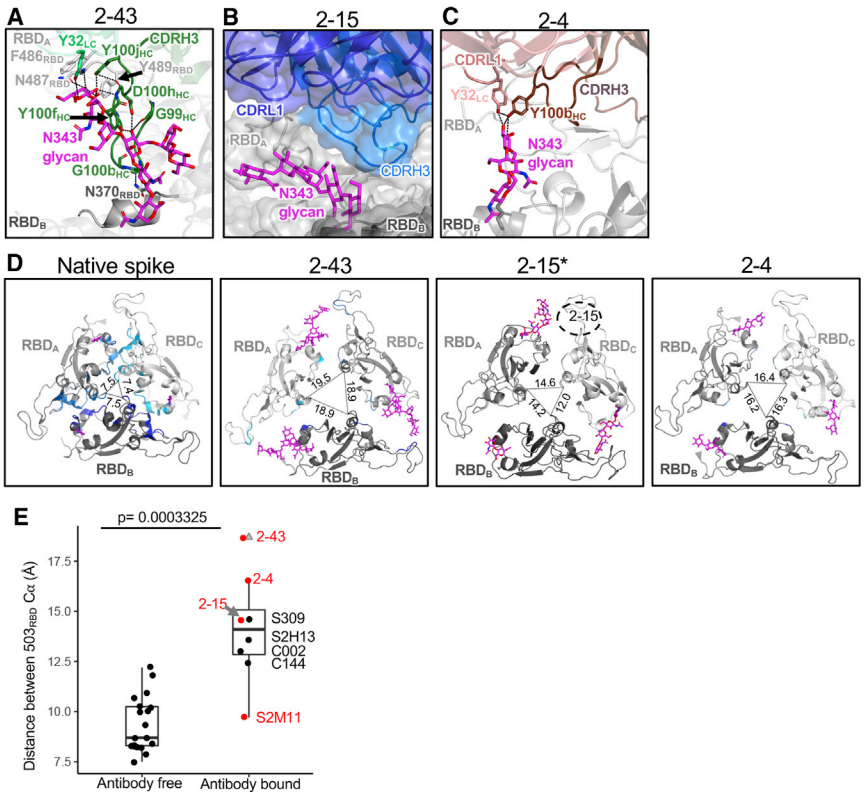

Figure 6. Subset of the VH1-2 antibody class uses an elongated CDRH3 to recognize the glycan N343 from a neighboring RBD, a quaternary interaction that expands the SARS-CoV-2 spike

(A) Close-up view of the quaternary epitope of 2-43. The 2-43 CDRH3 forms two hydrogen-bond networks (black dashed lines) with an adjacent RBD (RBD_B) N343 glycan and also interacts with helix 364–371 of RBD_B.

(B) Close-up view of potential quaternary interactions between 2-15 and the neighboring RBD (RBD_B). 2-15 reconstructed from cryo-EM data shows a minor quaternary interaction.

(C) Close-up view of the interaction between 2-4 and the N343 glycan of the neighboring RBD.

(D) Distance between antibody-free and antibody-bound trimeric RBDs. Antibody binding induces significantly larger expansion of the trimeric RBDs. The three RBDs are gray. Residues at the RBD interfaces are cyan, light blue, and blue for protomers RBD_A, RBD_B, and RBD_C. respectively. The distances between RBD protomers was measured using Cα of position 503. Note: because of low resolution, the interface residues between RBDs were not shown for the 2-15 bound spike. 2-15 (dashed circle) binds to protomer RBDC.

(E) Distance of Cα of position 503 between the trimeric down RBDs. Antibody-free spikes have a shorter distance than the antibody-bound spikes. For the boxplots, the middle lines are medians. The lower and upper hinges correspond to the first and third quartiles, respectively. The Mann-Whitney U test was used. Outliers are shown as gray triangles.

See also Figures S2, S3, and S6.

why they do not lock the trimeric RBDs in an all-down conformation.

To understand whether antibody binding induces conformation change in the SARS-CoV-2 spike protein, we compared the antibody-bound and ligand-free spike structures in the closed (all down) prefusion conformation. These comparisons showed that the binding of the VH1-2 antibodies (except S2M11), as well as other RBD-directed antibodies leads to significantly larger distances and less contacts between the trimeric down RBDs (Figures 6D and 6E). Each of these antibodies has a role in bridging the interactions between RBDs as well as in reorienting the conformation of the N343 glycan. However, antibodies like 2-15, which does not form strong interactions with the adjacent RBD, may disassemble the spike when three Fabs bind to the RBDs (Figures S2J and S2K). In addition, superposition of 2-15 on the down RBD in the ligand-free spike revealed the light chain to significantly clash with an adjacent up RBD (Figure S6D), suggesting members of the VH1-2 antibody class to either bind only down RBDs when a neighboring down RBD is available or push the neighboring up RBD away to bind down RBDs. Consistent with the first mechanism, we did not observe a neighboring up RBD adjacent to 2-15, and 2-4 bound down RBDs in the cryo-EM data. In contrast, C121 adopts the second mechanism through light-chain interaction with the adjacent up RBD (Figure S6D) (Barnes et al., 2020a).

In summary, the quaternary interaction and angle of approach determine that the VH1-2 antibody class modulates the SARS-CoV-2 spike conformation when binding to a down RBD.

DISCUSSION

In this study, we determined structures of three nAbs: 2-43, 2-15, and H4, which revealed a VH1-2 antibody class with a common RBD-binding mode and similar angles of approach. The VH1-2 antibody class uses two modules for spike recognition with the VH1-2-gene-encoded module for recognition of RBD and CDRH3 module for quaternary recognition. The VH1-2 antibody class has little or no restraint on CDRH3 length. The prevalence of the VH1-2 antibody class in numerous donors (Brouwer et al., 2020; Hansen et al., 2020; Ju et al., 2020; Kreer et al., 2020; Liu et al., 2020a; Robbiani et al., 2020; Rogers et al., 2020; Tortorici et al., 2020; Wu et al., 2020b; Zost et al., 2020) suggests it to be a common component of the effective antibody response to SARS-CoV-2, which can include highly potent neutralizing antibodies.

For some members of the VH1-2 class, recognition of a quaternary epitope can lock RBDs in the down conformation, providing an additional mechanism by which to achieve high neutralization potency. The quaternary epitopes of the VH1-2 class include the N343 glycan and helix 364–371 of an adjacent RBD. A similar quaternary epitope is recognized by the type-II

VH3-53/-66 class antibody C144 (Barnes et al., 2020a). Thus, this quaternary epitope appears to represent a supersite at which antibodies lock the RBDs in the all-down conformation. We also observe that the quaternary interaction can induce distinct conformational changes of the trimeric down RBDs. The quaternary interaction observed in S2M11 does not significantly alter the distance between spike protomers (Figure 4E) (Tortorici et al., 2020). In contrast, the quaternary interactions of 2-43 and 2-4, mediated predominantly by CDRH3, increase the distance of the trimeric RBDs (Figure 4). For 2-15, the cryo-EM structure of one Fab-bound spike revealed a CDRH3 conformation moving away from the adjacent down RBD to avoid a steric clash. Despite that, 2-15 also increases the distance among RBDs, which may be the result of mobile quaternary contacts that cannot be observed in the low-resolution cryo-EM reconstruction. We anticipate that the interactions among RBDs could be further weakened when all three protomers are bound by 2-15, which may be the cause of the observed spike disassembly by 2-15 (Figures S2J and S2K). The disassembly of the spike may be another mechanism for 2-15 to achieve ultrapotent neutralization. In addition, the crystal structure of 2-15 in complex with isolated RBDs showed 2-15 to have another stable binding mode in the absence of a quaternary contact. We hypothesize that this binding mode may be observed when 2-15 binds to up RBDs and cannot form quaternary interactions.

The structural information we present also provides clues for further optimization of the VH1-2 antibody class. Despite members of the class achieving high potency with germline gene-mediated interactions, we observe that somatic hypermutations can further improve this class significantly. The conserved mode of RBD recognition implies that members of the antibody class will be sensitive to similar viral escape mutations. In particular, $K417N_{RBD}$, $L452R_{RBD}$, $E484K_{RBD}$, and $N501Y_{RBD}$ mutations are observed in emerging SARS-CoV-2 variants (e.g., B.1.351, B.1.1.7, and B.1.429) with transmission rates dramatically higher than that of preexisting strains (Davies et al., 2021; Tegally et al., 2020). We found that positions 452 and 484 are within the VH1-2 antibody epitopes (Figure S3E). Mutation $E484K_{RBD}$, but not $K417N_{RBD}$ and $N501Y_{RBD}$, impairs both binding affinity and neutralization potency of the VH1-2 antibody class (Barnes et al., 2020a; Tortorici et al., 2020; Wang et al., 2021). We anticipate that $L452R_{RBD}$ will also impair the recognition by the VH1-2 antibody class, but further investigation is required to examine the hypothesis.

STAR★METHODS

Detailed methods are provided in the online version of this paper and include the following:

- KEY RESOURCES TABLE
- RESOURCE AVAILABILITY
  - Lead contact
  - Materials availability
  - Data and code availability
- EXPERIMENTAL MODEL AND SUBJECT DETAILS
- METHOD DETAILS
  - Expression and purification of SARS-CoV-2 spike and RBD proteins
  - Antibody production and mutagenesis
  - Production of Fab from IgG
  - IgG Surface Plasmon Resonance binding experiments
  - Pseudovirus neutralization assays
  - Antibody gene assignments and genetic analyses
  - Cryo-EM data collection and processing
  - Cryo-EM model building
  - X-ray data collection, structure solution, model building and refinement
  - Calculation of angle of approach
- QUANTIFICATION AND STATISTICAL ANALYSIS

SUPPLEMENTAL INFORMATION

Supplemental information can be found online at https://doi.org/10.1016/j.celrep.2021.108950.

ACKNOWLEDGMENTS

Cryo-EM data collection was performed at the National Center for Cryo-EM Access and Training and the Simons Electron Microscopy Center located at the New York Structural Biology Center, supported by the National Institutes of Health (NIH) Common Fund Transformative High Resolution Cryo-Electron Microscopy program (U24 GM129539) and by grants from the Simons Foundation (SF349247) and the NY State Assembly. Some of this work was also performed at the Columbia University Cryo-Electron Microscopy Center. Data analysis was performed at the National Resource for Automated Molecular Microscopy (NRAMM), supported by the NIH National Institute of General Medical Sciences (GM103310). We thank D. Neau, S. Banerjee, and Igor Kourinov for help with synchrotron data collection conducted at the Northeastern Collaborative Access Team 24-ID-C beamline, which is funded by the National Institute of General Medical Sciences from the NIH (P30 GM124165). This research used resources of the Advanced Photon Source, a US Department of Energy (DOE) Office of Science User Facility operated for the DOE Office of Science by Argonne National Laboratory under contract no. DE-AC02-06CH11357. Support for this work was provided by the Intramural Research Program of the Vaccine Research Center, National Institute of Allergy and Infectious Diseases (NIAID), NIH. This study was supported by Samuel Yin, Pony Ma, Peggy, Andrew Cherng, Brii Biosciences, Jack Ma Foundation, JBP Foundation, Carol Ludwig, and Roger and David Wu.

AUTHOR CONTRIBUTIONS

M.R. and G.C. determined the cryo-EM structures of 2-43, 2-15, and H4; Y.G. performed bioinformatics analyses; E.R.R. solved the crystal structure of 2-15; L.L. performed surface plasmon resonance (SPR) assay; P.W. performed the neutralization assessment; J.Y. produced antibodies; P.K. estimated binding affinity data from SPR; J.S.B., F.A.B., S.M.M., and B.Z. produced proteins; Y.H. and D.D.H. supervised antibody production, SPR, and neutralization assays; P.D.K. supervised reagents; L.S. supervised cryo-EM and crystal structure studies; Z.S. supervised the informatics studies. L.S. and Z.S. oversaw the project and, with M.R., Y.G., E.R., L.L., P.W., J.Y., and B.Z., wrote the manuscript, with all authors providing revisions and comments.

DECLARATION OF INTERESTS

D.D.H., Y.H., J.Y., L.L., and P.W. are inventors of a patent describing antibodies 2-43, 2-4, and 2-15 reported on here.

Received: December 31, 2020
Revised: February 1, 2021
Accepted: March 15, 2021
Published: March 19, 2021

REFERENCES

Adams, P.D., Gopal, K., Grosse-Kunstleve, R.W., Hung, L.W., Ioerger, T.R., McCoy, A.J., Moriarty, N.W., Pai, R.K., Read, R.J., Romo, T.D., et al. (2004). Recent developments in the PHENIX software for automated crystallographic structure determination. J. Synchrotron Radiat. *11*, 53–55.

Adams, P.D., Afonine, P.V., Bunkóczi, G., Chen, V.B., Davis, I.W., Echols, N., Headd, J.J., Hung, L.W., Kapral, G.J., Grosse-Kunstleve, R.W., et al. (2010). PHENIX: a comprehensive Python-based system for macromolecular structure solution. Acta Crystallogr. D Biol. Crystallogr. *66*, 213–221.

Afonine, P.V., Grosse-Kunstleve, R.W., Echols, N., Headd, J.J., Moriarty, N.W., Mustyakimov, M., Terwilliger, T.C., Urzhumtsev, A., Zwart, P.H., and Adams, P.D. (2012). Towards automated crystallographic structure refinement with phenix.refine. Acta Crystallogr. D Biol. Crystallogr. *68*, 352–367.

Bangaru, S., Ozorowski, G., Turner, H.L., Antanasijevic, A., Huang, D., Wang, X., Torres, J.L., Diedrich, J.K., Tian, J.H., Portnoff, A.D., et al. (2020). Structural analysis of full-length SARS-CoV-2 spike protein from an advanced vaccine candidate. Science *370*, 1089–1094.

Barad, B.A., Echols, N., Wang, R.Y., Cheng, Y., DiMaio, F., Adams, P.D., and Fraser, J.S. (2015). EMRinger: side chain-directed model and map validation for 3D cryo-electron microscopy. Nat. Methods *12*, 943–946.

Barnes, C.O., Jette, C.A., Abernathy, M.E., Dam, K.A., Esswein, S.R., Gristick, H.B., Malyutin, A.G., Sharaf, N.G., Huey-Tubman, K.E., Lee, Y.E., et al. (2020a). SARS-CoV-2 neutralizing antibody structures inform therapeutic strategies. Nature *588*, 682–687.

Barnes, C.O., West, A.P., Jr., Huey-Tubman, K.E., Hoffmann, M.A.G., Sharaf, N.G., Hoffman, P.R., Koranda, N., Gristick, H.B., Gaebler, C., Muecksch, F., et al. (2020b). Structures of human antibodies bound to SARS-CoV-2 spike reveal common epitopes and recurrent features of antibodies. Cell *182*, 828–842.e16.

Brochet, X., Lefranc, M.P., and Giudicelli, V. (2008). IMGT/V-QUEST: the highly customized and integrated system for IG and TR standardized V-J and V-D-J sequence analysis. Nucleic Acids Res. *36*, W503-8.

Brouwer, P.J.M., Caniels, T.G., van der Straten, K., Snitselaar, J.L., Aldon, Y., Bangaru, S., Torres, J.L., Okba, N.M.A., Claireaux, M., Kerster, G., et al. (2020). Potent neutralizing antibodies from COVID-19 patients define multiple targets of vulnerability. Science *369*, 643–650.

Cai, Y., Zhang, J., Xiao, T., Peng, H., Sterling, S.M., Walsh, R.M., Rawson, S., Rits-Volloch, S., and Chen, B. (2020). Distinct conformational states of SARS-CoV-2 spike protein. Science, eabd4251.

Cao, Y., Su, B., Guo, X., Sun, W., Deng, Y., Bao, L., Zhu, Q., Zhang, X., Zheng, Y., Geng, C., et al. (2020). Potent Neutralizing Antibodies against SARS-CoV-2 Identified by High-Throughput Single-Cell Sequencing of Convalescent Patients' B Cells. Cell *182*, 73–84.e16.

Chen, V.B., Arendall, W.B., III, Headd, J.J., Keedy, D.A., Immormino, R.M., Kapral, G.J., Murray, L.W., Richardson, J.S., and Richardson, D.C. (2010). MolProbity: all-atom structure validation for macromolecular crystallography. Acta Crystallogr. D Biol. Crystallogr. *66*, 12–21.

Chen, P., Nirula, A., Heller, B., Gottlieb, R.L., Boscia, J., Morris, J., Huhn, G., Cardona, J., Mocherla, B., Stosor, V., et al. (2020). SARS-CoV-2 neutralizing antibody LY-CoV555 in outpatients with Covid-19. N. Engl. J. Med. *384*, 229–237.

Collaborative Computational Project, Number 4 (1994). The CCP4 suite: programs for protein crystallography. Acta Crystallogr. D Biol. Crystallogr. *50*, 760–763.

Croll, T.I. (2018). ISOLDE: a physically realistic environment for model building into low-resolution electron-density maps. Acta Crystallogr. D Struct. Biol. *74*, 519–530.

Davies, N., Barnard, C.R., Jarvis, I.C., Kucharski, J.A., Munday, D.J., Pearson, A.B.C., Russell, W.T., Tully, D.C., Abbott, S., Gimma, A., et al. (2021). Estimated transmissibility and severity of novel SARS-CoV-2 variant of concern 202012/01 in England. medRxiv. https://doi.org/10.1101/2021.02.01.21250959.

Davis, I.W., Murray, L.W., Richardson, J.S., and Richardson, D.C. (2004). MOLPROBITY: structure validation and all-atom contact analysis for nucleic acids and their complexes. Nucleic Acids Res. *32*, W615-9.

Diemert, D., and McElrath, J. (2018). A phase I trial to evaluate the safety and immunogenicity of eOD-GT8 60mer vaccine, adjuvanted. ClinicalTrials.gov.

Dong, E., Du, H., and Gardner, L. (2020). An interactive web-based dashboard to track COVID-19 in real time. Lancet Infect. Dis. *20*, 533–534.

Du, S., Cao, Y., Zhu, Q., Yu, P., Qi, F., Wang, G., Du, X., Bao, L., Deng, W., Zhu, H., et al. (2020). Structurally Resolved SARS-CoV-2 Antibody Shows High Efficacy in Severely Infected Hamsters and Provides a Potent Cocktail Pairing Strategy. Cell *183*, 1013–1023.e13.

Edgar, R.C. (2004). MUSCLE: multiple sequence alignment with high accuracy and high throughput. Nucleic Acids Res. *32*, 1792–1797.

Ehrhardt, S.A., Zehner, M., Krähling, V., Cohen-Dvashi, H., Kreer, C., Elad, N., Gruell, H., Ercanoglu, M.S., Schommers, P., Gieselmann, L., et al. (2019). Polyclonal and convergent antibody response to Ebola virus vaccine rVSV-ZEBOV. Nat. Med. *25*, 1589–1600.

Emsley, P., and Cowtan, K. (2004). Coot: model-building tools for molecular graphics. Acta Crystallogr. D Biol. Crystallogr. *60*, 2126–2132.

Emsley, P., Lohkamp, B., Scott, W.G., and Cowtan, K. (2010). Features and development of Coot. Acta Crystallogr. D Biol. Crystallogr. *66*, 486–501.

Evans, P. (2006). Scaling and assessment of data quality. Acta Crystallogr. D Biol. Crystallogr. *62*, 72–82.

Goddard, T.D., Huang, C.C., Meng, E.C., Pettersen, E.F., Couch, G.S., Morris, J.H., and Ferrin, T.E. (2018). UCSF ChimeraX: meeting modern challenges in visualization and analysis. Protein Sci. *27*, 14–25.

Han, Y., Duan, X., Yang, L., Nilsson-Payant, B.E., Wang, P., Duan, F., Tang, X., Yaron, T.M., Zhang, T., Uhl, S., et al. (2021). Identification of SARS-CoV-2 inhibitors using lung and colonic organoids. Nature *589*, 270–275.

Hansen, J., Baum, A., Pascal, K.E., Russo, V., Giordano, S., Wloga, E., Fulton, B.O., Yan, Y., Koon, K., Patel, K., et al. (2020). Studies in humanized mice and convalescent humans yield a SARS-CoV-2 antibody cocktail. Science *369*, 1010–1014.

Haynes, B.F., Kelsoe, G., Harrison, S.C., and Kepler, T.B. (2012). B-cell-lineage immunogen design in vaccine development with HIV-1 as a case study. Nat. Biotechnol. *30*, 423–433.

Henderson, R., Edwards, R.J., Mansouri, K., Janowska, K., Stalls, V., Gobeil, S.M.C., Kopp, M., Li, D., Parks, R., Hsu, A.L., et al. (2020). Controlling the SARS-CoV-2 spike glycoprotein conformation. Nat. Struct. Mol. Biol. *27*, 925–933.

Herrera, N.G., Morano, N.C., Celikgil, A., Georgiev, G.I., Malonis, R.J., Lee, J.H., Tong, K., Vergnolle, O., Massimi, A.B., Yen, L.Y., et al. (2020). Characterization of the SARS-CoV-2 S Protein: Biophysical, Biochemical, Structural, and Antigenic Analysis. ACS Omega *6*, 85–102.

Hoffmann, M., Kleine-Weber, H., Schroeder, S., Krüger, N., Herrler, T., Erichsen, S., Schiergens, T.S., Herrler, G., Wu, N.H., Nitsche, A., et al. (2020). SARS-CoV-2 Cell Entry Depends on ACE2 and TMPRSS2 and Is Blocked by a Clinically Proven Protease Inhibitor. Cell *181*, 271–280.e8.

Huo, J., Zhao, Y., Ren, J., Zhou, D., Duyvesteyn, H.M.E., Ginn, H.M., Carrique, L., Malinauskas, T., Ruza, R.R., Shah, P.N.M., et al. (2020). Neutralization of SARS-CoV-2 by Destruction of the Prefusion Spike. Cell Host Microbe *28*, 445–454.e6.

Hurlburt, N.K., Seydoux, E., Wan, Y.H., Edara, V.V., Stuart, A.B., Feng, J., Suthar, M.S., McGuire, A.T., Stamatatos, L., and Pancera, M. (2020). Structural basis for potent neutralization of SARS-CoV-2 and role of antibody affinity maturation. Nat. Commun. *11*, 5413.

Imkeller, K., Scally, S.W., Bosch, A., Martí, G.P., Costa, G., Triller, G., Murugan, R., Renna, V., Jumaa, H., Kremsner, P.G., et al. (2018). Antihomotypic affinity maturation improves human B cell responses against a repetitive epitope. Science *360*, 1358–1362.

Jardine, J., Julien, J.P., Menis, S., Ota, T., Kalyuzhniy, O., McGuire, A., Sok, D., Huang, P.S., MacPherson, S., Jones, M., et al. (2013). Rational HIV

immunogen design to target specific germline B cell receptors. Science *340*, 711–716.

Joosten, R.P., Long, F., Murshudov, G.N., and Perrakis, A. (2014). The PDB_REDO server for macromolecular structure model optimization. IUCrJ *1*, 213–220.

Joyce, M.G., Wheatley, A.K., Thomas, P.V., Chuang, G.-Y., Soto, C., Bailer, R.T., Druz, A, Georgiev, I.S, Gillespie, R.A, Kanekiyo, M, et al. (2016). Vaccine-induced antibodies that neutralize group 1 and group 2 influenza A viruses. Cell *166*, 609–623.

Ju, B., Zhang, Q., Ge, J., Wang, R., Sun, J., Ge, X., Yu, J., Shan, S., Zhou, B., Song, S., et al. (2020). Human neutralizing antibodies elicited by SARS-CoV-2 infection. Nature *584*, 115–119.

Kabsch, W. (2010). Integration, scaling, space-group assignment and post-refinement. Acta Crystallogr. D Biol. Crystallogr. *66*, 133–144.

Kallewaard, N.L., Corti, D., Collins, P.J., Neu, U., McAuliffe, J.M., Benjamin, E., Wachter-Rosati, L., Palmer-Hill, F.J., Yuan, A.Q., Walker, P.A., et al. (2016). Structure and function analysis of an antibody recognizing all influenza A subtypes. Cell *166*, 596–608.

Kreer, C., Zehner, M., Weber, T., Ercanoglu, M.S., Gieselmann, L., Rohde, C., Halwe, S., Korenkov, M., Schommers, P., Vanshylla, K., et al. (2020). Longitudinal isolation of potent near-germline SARS-CoV-2-neutralizing antibodies from COVID-19 patients. Cell *182*, 843–854.e12.

Kreye, J., Reincke, S.M., Kornau, H.C., Sánchez-Sendin, E., Corman, V.M., Liu, H., Yuan, M., Wu, N.C., Zhu, X., Lee, C.D., et al. (2020). A Therapeutic Non-self-reactive SARS-CoV-2 Antibody Protects from Lung Pathology in a COVID-19 Hamster Model. Cell *183*, 1058–1069.e19.

Krissinel, E., and Henrick, K. (2007). Inference of macromolecular assemblies from crystalline state. J. Mol. Biol. *372*, 774–797.

Kwong, P.D., and Mascola, J.R. (2012). Human antibodies that neutralize HIV-1: identification, structures, and B cell ontogenies. Immunity *37*, 412–425.

Kwong, P.D., and Mascola, J.R. (2018). HIV-1 vaccines based on antibody identification, B cell ontogeny, and epitope structure. Immunity *48*, 855–871.

Leem, J., Dunbar, J., Georges, G., Shi, J., and Deane, C.M. (2016). ABodyBuilder: automated antibody structure prediction with data-driven accuracy estimation. MAbs *8*, 1259–1268.

Lefranc, M.P., Giudicelli, V., Ginestoux, C., Jabado-Michaloud, J., Folch, G., Bellahcene, F., Wu, Y., Gemrot, E., Brochet, X., Lane, J., et al. (2009). IMGT, the international ImMunoGeneTics information system. Nucleic Acids Res. *37*, D1006–D1012.

Liu, L., Wang, P., Nair, M.S., Yu, J., Rapp, M., Wang, Q., Luo, Y., Chan, J.F., Sahi, V., Figueroa, A., et al. (2020a). Potent neutralizing antibodies against multiple epitopes on SARS-CoV-2 spike. Nature *584*, 450–456.

Liu, H., Wu, N.C., Yuan, M., Bangaru, S., Torres, J.L., Caniels, T.G., van Schooten, J., Zhu, X., Lee, C.-C.D., Brouwer, P.J.M., et al. (2020b). Cross-neutralization of a SARS-CoV-2 antibody to a functionally conserved site is mediated by avidity. Immunity *53*, 1272–1280.e5.

Lv, Z., Deng, Y.Q., Ye, Q., Cao, L., Sun, C.Y., Fan, C., Huang, W., Sun, S., Sun, Y., Zhu, L., et al. (2020). Structural basis for neutralization of SARS-CoV-2 and SARS-CoV by a potent therapeutic antibody. Science *369*, 1505–1509.

McCallum, M., Walls, A.C., Bowen, J.E., Corti, D., and Veesler, D. (2020). Structure-guided covalent stabilization of coronavirus spike glycoprotein trimers in the closed conformation. Nat. Struct. Mol. Biol. *27*, 942–949.

McCoy, A.J., Grosse-Kunstleve, R.W., Adams, P.D., Winn, M.D., Storoni, L.C., and Read, R.J. (2007). Phaser crystallographic software. J. Appl. Cryst. *40*, 658–674.

Pappas, L., Foglierini, M., Piccoli, L., Kallewaard, N.L., Turrini, F., Silacci, C., Fernandez-Rodriguez, B., Agatic, G., Giacchetto-Sasselli, I., Pellicciotta, G., et al. (2014). Rapid development of broadly influenza neutralizing antibodies through redundant mutations. Nature *516*, 418–422.

Pettersen, E.F., Goddard, T.D., Huang, C.C., Couch, G.S., Greenblatt, D.M., Meng, E.C., and Ferrin, T.E. (2004). UCSF chimera—a visualization system for exploratory research and analysis. J. Comput. Chem. *25*, 1605–1612.

Pinto, D., Park, Y.-J., Beltramello, M., Walls, A.C., Tortorici, M.A., Bianchi, S., Jaconi, S., Culap, K., Zatta, F., De Marco, A., et al. (2020a). Structural and functional analysis of a potent sarbecovirus neutralizing antibody. bioRxiv, 2020.2004.2007.023903.

Pinto, D., Park, Y.J., Beltramello, M., Walls, A.C., Tortorici, M.A., Bianchi, S., Jaconi, S., Culap, K., Zatta, F., De Marco, A., et al. (2020b). Cross-neutralization of SARS-CoV-2 by a human monoclonal SARS-CoV antibody. Nature *583*, 290–295.

Punjani, A., Rubinstein, J.L., Fleet, D.J., and Brubaker, M.A. (2017). cryoSPARC: algorithms for rapid unsupervised cryo-EM structure determination. Nat. Methods *14*, 290–296.

Robbiani, D.F., Gaebler, C., Muecksch, F., Lorenzi, J.C.C., Wang, Z., Cho, A., Agudelo, M., Barnes, C.O., Gazumyan, A., Finkin, S., et al. (2020). Convergent antibody responses to SARS-CoV-2 in convalescent individuals. Nature *584*, 437–442.

Rogers, T.F., Zhao, F., Huang, D., Beutler, N., Burns, A., He, W.T., Limbo, O., Smith, C., Song, G., Woehl, J., et al. (2020). Isolation of potent SARS-CoV-2 neutralizing antibodies and protection from disease in a small animal model. Science *369*, 956–963.

Schmidt, A.G., Xu, H., Khan, A.R., O'Donnell, T., Khurana, S., King, L.R., Manischewitz, J., Golding, H., Suphaphiphat, P., Carfi, A., et al. (2013). Preconfiguration of the antigen-binding site during affinity maturation of a broadly neutralizing influenza virus antibody. Proc. Natl. Acad. Sci. USA *110*, 264–269.

Schramm, C.A., Sheng, Z., Zhang, Z., Mascola, J.R., Kwong, P.D., and Shapiro, L. (2016). SONAR: a high-throughput pipeline for inferring antibody ontogenies from longitudinal sequencing of B cell transcripts. Front. Immunol. *7*, 372.

Shi, R., Shan, C., Duan, X., Chen, Z., Liu, P., Song, J., Song, T., Bi, X., Han, C., Wu, L., et al. (2020). A human neutralizing antibody targets the receptor-binding site of SARS-CoV-2. Nature *584*, 120–124. https://doi.org/10.1038/s41586-41020-42381-y.

Sievers, F., and Higgins, D.G. (2018). Clustal Omega for making accurate alignments of many protein sequences. Protein Sci. *27*, 135–145.

Suloway, C., Pulokas, J., Fellmann, D., Cheng, A., Guerra, F., Quispe, J., Stagg, S., Potter, C.S., and Carragher, B. (2005). Automated molecular microscopy: the new Leginon system. J. Struct. Biol. *151*, 41–60.

Tegally, H., Wilkinson, E., Giovanetti, M., Iranzadeh, A., Fonseca, V., Giandhari, J., Doolabh, D., Pillay, S., San, E.J., Msomi, N., et al. (2020). Emergence and rapid spread of a new severe acute respiratory syndrome-related coronavirus 2 (SARS-CoV-2) lineage with multiple spike mutations in South Africa. medRxiv, 2020.2012.2021.20248640.

Toelzer, C., Gupta, K., Yadav, S.K.N., Borucu, U., Davidson, A.D., Kavanagh Williamson, M., Shoemark, D.K., Garzoni, F., Staufer, O., Milligan, R., et al. (2020). Free fatty acid binding pocket in the locked structure of SARS-CoV-2 spike protein. Science *370*, 725–730.

Tortorici, M.A., Beltramello, M., Lempp, F.A., Pinto, D., Dang, H.V., Rosen, L.E., McCallum, M., Bowen, J., Minola, A., Jaconi, S., et al. (2020). Ultrapotent human antibodies protect against SARS-CoV-2 challenge via multiple mechanisms. Science *370*, 950–957.

Walls, A.C., Park, Y.J., Tortorici, M.A., Wall, A., McGuire, A.T., and Veesler, D. (2020). Structure, Function, and Antigenicity of the SARS-CoV-2 Spike Glycoprotein. Cell *181*, 281–292.e6.

Wang, Q., Zhang, Y., Wu, L., Niu, S., Song, C., Zhang, Z., Lu, G., Qiao, C., Hu, Y., Yuen, K.Y., et al. (2020). Structural and functional basis of SARS-CoV-2 entry by using human ACE2. Cell *181*, 894–904.e9.

Wang, P., Liu, L., Iketani, S., Luo, Y., Guo, Y., Wang, M., Yu, J., Zhang, B., Kwong, P.D., Graham, B.S., et al. (2021). Increased resistance of SARS-CoV-2 variants B.1.351 and B.1.1.7 to antibody neutralization. bioRxiv, 2021.2001.2025.428137.

Winn, M.D., Ballard, C.C., Cowtan, K.D., Dodson, E.J., Emsley, P., Evans, P.R., Keegan, R.M., Krissinel, E.B., Leslie, A.G., McCoy, A., et al. (2011). Overview of the CCP4 suite and current developments. Acta Crystallogr. D Biol. Crystallogr. *67*, 235–242.

Wrapp, D., Wang, N., Corbett, K.S., Goldsmith, J.A., Hsieh, C.L., Abiona, O., Graham, B.S., and McLellan, J.S. (2020). Cryo-EM structure of the 2019-nCoV spike in the prefusion conformation. Science *367*, 1260–1263.

Wrobel, A.G., Benton, D.J., Xu, P., Roustan, C., Martin, S.R., Rosenthal, P.B., Skehel, J.J., and Gamblin, S.J. (2020). SARS-CoV-2 and bat RaTG13 spike glycoprotein structures inform on virus evolution and furin-cleavage effects. Nat. Struct. Mol. Biol. *27*, 763–767.

Wu, N.C., Yuan, M., Liu, H., Lee, C.D., Zhu, X., Bangaru, S., Torres, J.L., Caniels, T.G., Brouwer, P.J.M., van Gils, M.J., et al. (2020a). An alternative binding mode of IGHV3-53 antibodies to the SARS-CoV-2 receptor binding domain. Cell Rep. *33*, 108274.

Wu, Y., Wang, F., Shen, C., Peng, W., Li, D., Zhao, C., Li, Z., Li, S., Bi, Y., Yang, Y., et al. (2020b). A noncompeting pair of human neutralizing antibodies block COVID-19 virus binding to its receptor ACE2. Science *368*, 1274–1278.

Xiong, X., Qu, K., Ciazynska, K.A., Hosmillo, M., Carter, A.P., Ebrahimi, S., Ke, Z., Scheres, S.H.W., Bergamaschi, L., Grice, G.L., et al.; CITIID-NIHR COVID-19 BioResource Collaboration (2020). A thermostable, closed SARS-CoV-2 spike protein trimer. Nat. Struct. Mol. Biol. *27*, 934–941.

Yao, H., Sun, Y., Deng, Y.-Q., Wang, N., Tan, Y., Zhang, N.-N., Li, X.-F., Kong, C., Xu, Y.-P., Chen, Q., et al. (2021). Rational development of a human antibody cocktail that deploys multiple functions to confer Pan-SARS-CoVs protection. Cell Res. *31*, 25–36.

Ye, J., Ma, N., Madden, T.L., and Ostell, J.M. (2013). IgBLAST: an immunoglobulin variable domain sequence analysis tool. Nucleic Acids Res. *41*, W34-40.

Yuan, M., Liu, H., Wu, N.C., Lee, C.D., Zhu, X., Zhao, F., Huang, D., Yu, W., Hua, Y., Tien, H., et al. (2020). Structural basis of a shared antibody response to SARS-CoV-2. Science *369*, 1119–1123.

Zhou, T., Zhu, J., Wu, X., Moquin, S., Zhang, B., Acharya, P., Georgiev, I.S., Altae-Tran, H.R., Chuang, G.Y., Joyce, M.G., et al.; NISC Comparative Sequencing Program (2013). Multidonor analysis reveals structural elements, genetic determinants, and maturation pathway for HIV-1 neutralization by VRC01-class antibodies. Immunity *39*, 245–258.

Zhou, T., Lynch, R.M., Chen, L., Acharya, P., Wu, X., Doria-Rose, N.A., Joyce, M.G., Lingwood, D., Soto, C., Bailer, R.T., et al.; NISC Comparative Sequencing Program (2015). Structural repertoire of HIV-1-neutralizing antibodies targeting the CD4 supersite in 14 donors. Cell *161*, 1280–1292.

Zhou, P., Yang, X.L., Wang, X.G., Hu, B., Zhang, L., Zhang, W., Si, H.R., Zhu, Y., Li, B., Huang, C.L., et al. (2020). A pneumonia outbreak associated with a new coronavirus of probable bat origin. Nature *579*, 270–273.

Zhu, K., Day, T., Warshaviak, D., Murrett, C., Friesner, R., and Pearlman, D. (2014). Antibody structure determination using a combination of homology modeling, energy-based refinement, and loop prediction. Proteins *82*, 1646–1655.

Zhu, N., Zhang, D., Wang, W., Li, X., Yang, B., Song, J., Zhao, X., Huang, B., Shi, W., Lu, R., et al.; China Novel Coronavirus Investigating and Research Team (2020). A novel coronavirus from patients with pneumonia in China, 2019. N. Engl. J. Med. *382*, 727–733.

Zost, S.J., Gilchuk, P., Case, J.B., Binshtein, E., Chen, R.E., Nkolola, J.P., Schäfer, A., Reidy, J.X., Trivette, A., Nargi, R.S., et al. (2020). Potently neutralizing and protective human antibodies against SARS-CoV-2. Nature *584*, 443–449.

STAR★METHODS

KEY RESOURCES TABLE

REAGENT or RESOURCE	SOURCE	IDENTIFIER
Antibodies		
2-43	Liu et al., 2020b	N/A
2-15	Liu et al., 2020b	N/A
2-4	Liu et al., 2020b	N/A
H4	Wu et al., 2020b	N/A
anti-VSV-G antibody	ATCC	Cat#CRL-2700; RRID:CVCL_G654
Bacteria and virus strains		
SARS-CoV-2 pseudovirus	Liu et al., 2020b	N/A
Chemicals, peptides, and recombinant proteins		
polyethylenimine	Polysciences, Inc.	Cat# 23966
Turbo293	Speed BioSystems	Cat#PXX1002
HRV-3C protease	MilliporeSigma	Cat# SAE0045
SARS-CoV-2 spike S2P	Wrapp et al., 2020	N/A
SARS-CoV-2 spike	provided by Dr. Peihui Wang, China	N/A
SARS-CoV-2 RBD	This study	N/A
Critical commercial assays		
Strep-Tactin XT Superflow 50%	Zymo research	Cat#P2004-1-5
Sensor Chip CM5	Cytiva	Cat#BR100030
His Capture Kit	Cytiva	Cat#28995056
Glycine 1.5	Cytiva	Cat# BR100354
HBS-EP+ Buffer	Cytiva	Cat# BR100826
QuikChange II site directed mutagenesis kit	Agilent	Cat# 200524
rProtein A Sepharose	GE	Cat#17-1279-01
NI-NTA	GE Health care	Cat# 17-0921-09
Superdex 200 Increase 10/300 GL	Cytiva	Cat# 28990945
Pierce Fab Preparation Kit	Thermo fisher	Cat# 44985
Deposited data		
New IGVL2-14 gene allele (IGVL2-14*0X)	This study	ENA: PRJEB31020
Cryo-EM structures: SARS-CoV-2 spike	Walls et al., 2020	PDB ID: 6VXX
Cryo-EM structures: SARS-CoV-2 spike	Henderson et al., 2020	PDB ID: 6X2C
Cryo-EM structures: SARS-CoV-2 spike	Herrera et al., 2020	PDB ID: 6X6P
Cryo-EM structures: SARS-CoV-2 spike	Henderson et al., 2020	PDB ID: 6X29
Cryo-EM structures: SARS-CoV-2 spike	McCallum et al., 2020	PDB ID: 6X79
Cryo-EM structures: SARS-CoV-2 spike	Zhou et al., 2020	PDB ID: 6XLU
Cryo-EM structures: SARS-CoV-2 spike	Zhou et al., 2020	PDB ID: 6XM5
Cryo-EM structures: SARS-CoV-2 spike	Cai et al., 2020	PDB ID: 6XR8
Cryo-EM structures: SARS-CoV-2 spike	Toelzer et al., 2020	PDB ID: 6ZB4
Cryo-EM structures: SARS-CoV-2 spike	Wrobel et al., 2020	PDB ID: 6ZGE
Cryo-EM structures: SARS-CoV-2 spike	Wrobel et al., 2020	PDB ID: 6ZGI
Cryo-EM structures: SARS-CoV-2 spike	Xiong et al., 2020	PDB ID: 6ZOX
Cryo-EM structures: SARS-CoV-2 spike	Xiong et al., 2020	PDB ID: 6ZOY
Cryo-EM structures: SARS-CoV-2 spike	Xiong et al., 2020	PDB ID: 6ZOZ
Cryo-EM structures: SARS-CoV-2 spike	Xiong et al., 2020	PDB ID: 6ZP0

(*Continued on next page*)

Continued

REAGENT or RESOURCE	SOURCE	IDENTIFIER
Cryo-EM structures: SARS-CoV-2 spike	Xiong et al., 2020	PDB ID: 6ZP1
Cryo-EM structures: SARS-CoV-2 spike	Xiong et al., 2020	PDB ID: 6ZP2
Cryo-EM structures: SARS-CoV-2 spike	Bangaru et al., 2020	PDB ID: 7JJI
Cryo-EM structures: SARS-CoV-2 spike	Wrobel et al., 2020	PDB ID: 6ZGG
Crystal structure: SARS-CoV-2 RBD	Wu et al., 2020b	PDB ID: 7BZ5
Crystal structure: CH65 UCA	Schmidt et al., 2013	PDB ID: 4HK0
Cryo-EM structure: 2-4	Liu et al., 2020b	PDB ID: 6XEY
Cryo-EM structure: S2M11	Tortorici et al., 2020	PDB ID:7K43
Cryo-EM structure: C121	Barnes et al., 2020a	PDB ID: 7K8X
Cryo-EM structure: C002	Barnes et al., 2020a	PDB ID: 7K8T
Cryo-EM structure: C144	Barnes et al., 2020a	PDB ID: 7K90
Cryo-EM structure: BD23	Cao et al., 2020	PDB ID: 7BYR
Cryo-EM structure: B38	Wu et al., 2020b	PDB ID: 7BZ5
Cryo-EM structure: S2H13	Tortorici et al., 2020	PDB ID: 7JV2
Cryo-EM structure: S309	Pinto et al., 2020a	PDB ID: 6WPS
Cryo-EM structure: C119	Barnes et al., 2020a	PDB ID: 7K8W
Cryo-EM structure: C102	Barnes et al., 2020a	PDB ID: 7K8M
Cryo-EM structure: C104	Barnes et al., 2020a	PDB ID: 7K8U
Cryo-EM structure: C110	Barnes et al., 2020a	PDB ID: 7K8V
Cryo-EM structure: S2E12	Tortorici et al., 2020	PDB ID:7K45
Cryo-EM structure: C135	Barnes et al., 2020a	PDB ID: 7K8Z
Cryo-EM structure: COVA1-16	Liu et al., 2020a	PDB ID: 7JMW
Cryo-EM structure: P17	Yao et al., 2021	PDB ID: 7CWO
Crystal structure: BD-236	Du et al., 2020	PDB ID: 7CHB
Crystal structure: BD-368-2	Du et al., 2020	PDB ID: 7CHE
Crystal structure: BD-629	Du et al., 2020	PDB ID: 7CH5
Crystal structure: P2C-1F11	Wang et al., 2020	PDB ID: 7CDI
Crystal structure: P2D-1A3	Wang et al., 2020	PDB ID: 7CDJ
Crystal structure: EY6A	Zhou et al., 2020	PDB ID: 6ZER
Crystal structure: CV07-250	Kreye et al., 2020	PDB ID: 6XKQ
Crystal structure: CV07-270	Kreye et al., 2020	PDB ID: 6XKP
Cryo-EM structure: S309	Pinto et al., 2020b	PDB ID: 6WPT
Crystal structure: P2B-2F6	Ju et al., 2020	PDB ID: 7BWJ
Crystal structure: CB6	Shi et al., 2020	PDB ID: 7C01
Cryo-EM structure: BD-23	Cao et al., 2020	PDB ID: 7BYR
Crystal structure: B38	Wu et al., 2020b	PDB ID: 7BZ5
Crystal structure: COVA2-39	Wu et al., 2020a	PDB ID: 7JMP
Crystal structure: COVA2-04	Wu et al., 2020a	PDB ID: 7JMO
Crystal structure: H014	Lv et al., 2020	PDB ID: 7CAH
Crystal structure: CR3022	Huo et al., 2020	PDB ID: 6YM0
Crystal structure: CV30	Hurlburt et al., 2020	PDB ID: 6XE1
Cryo-EM structure: REGN10933	Hansen et al., 2020	PDB ID: 6XDG
Cryo-EM structure: REGN10987	Hansen et al., 2020	PDB ID: 6XDG
Cryo-EM structure: C105	Barnes et al., 2020b	PDB ID: 6XCN
Cryo-EM structure: CC12.1	Yuan et al., 2020	PDB ID: 6XC2
Cryo-EM structure: CC12.3	Yuan et al., 2020	PDB ID: 6XC4
Crystal structure: 2-15	This study	PDB ID: 7L5B

(*Continued on next page*)

Continued

REAGENT or RESOURCE	SOURCE	IDENTIFIER
Cryo-EM structure: 2-43	This study	PDB ID: 7L56; EMDB-23165
Cryo-EM structure: 2-15	This study	PDB ID: 7L57; EMDB-23166
Cryo-EM structure: H4	This study	PDB ID: 7L58; EMDB-23167
Experimental models: Cell lines		
Expi293	ThermoFisher	Cat#A14527; RRID:CVCL_D615
HEK293T/17	ATCC	Cat# CRL-11268; RRID:CVCL_1926
Vero E6	ATCC	Cat# CRL-1586; RRID:CVCL_0574
Expi293F GnTI- Cells	Thermo Fisher	Cat# A39240
Recombinant DNA		
pVRC8400 vector	https://www.addgene.org	Cat#63160; RRID:Addgene_63164
gWiz	Aldeveron	Cat# 5008
pcDNA3.4	ThermoFisher	Cat# A14697
Software and algorithms		
GraphPad Prism 7.01 Software	GraphPad Prism Software, Inc.	N/A
The PyMol Molecular Graphics System, v1.8.6	Schrödinger, LLC	https://pymol.org/2/
IMGT/V-Quest	IMGT	http://www.imgt.org/IMGT_vquest/vquest
SONAR	Schramm et al., 2016	https://github.com/scharch/SONAR
Muscle	Edgar, 2004	https://drive5.com/usearch/
CLUSTALO	Sievers and Higgins, 2018	http://clustal.org/omega/
Python v3.8.3	https://www.python.org/downloads/	N/A
cryoSPARC, v2.15.0	Punjani et al., 2017	https://cryosparc.com/
UCSF Chimera, v1.14	Pettersen et al., 2004	https://www.cgl.ucsf.edu/chimera/
UCSF ChimeraX, v1.1	Goddard et al., 2018	https://www.cgl.ucsf.edu/chimerax/
Schrödinger Release 2020-2:BioLuminate	Zhu et al., 2014	https://www.schrodinger.com/products/bioluminate
ISOLDE, v.1.0.1	Croll, 2018	https://isolde.cimr.cam.ac.uk/
COOT, 0.9	Emsley et al., 2010	https://www2.mrc-lmb.cam.ac.uk/personal/pemsley/coot/
Phenix, v1.18	Adams et al., 2010	https://www.phenix-online.org/;
Leginon, v.3.5beta	Suloway et al., 2005	N/A
XDS	Kabsch, 2010	https://xds.mpimf-heidelberg.mpg.de/
CCP4i (Aimless)	Winn et al., 2011	https://www.ccp4.ac.uk
PDB-redo	Joosten et al., 2014	https://pdb-redo.eu/
MolProbity	Chen et al., 2010	http://molprobity.biochem.duke.edu
Other		
Free style Media	Invitrogen	Cat # 12338026

RESOURCE AVAILABILITY

Lead contact

Further information and requests for resources and reagents should be directed to and will be fulfilled by the Lead Contact, Zizhang Sheng (zs2248@cumc.columbia.edu).

Materials availability

Expression plasmids generated in this study for expressing SARS-CoV-2 proteins and antibody mutants will be shared upon request.

Data and code availability

Cryo-EM maps and fitted coordinates of 2-43, H4, and 2-15 were deposited to the EMDB (2-43: EMDB-23165; H4: EMDB-23167; 2-15: EMDB-23166) and RCSB (2-43: 7L56; H4: 7L58; 2-15: 7L57 and 7L5B) respectively. The new IGVL2-14 gene allele (IGVL2-14*0X)

was deposited to European Nucleotide Archive (ENA): PRJEB31020. All deposited data will be available upon publication of the study.

EXPERIMENTAL MODEL AND SUBJECT DETAILS

Expi293 cells and Expi293F GnTI- Cells were from ThermoFisher Scientific Inc (ThermoFisher, cat#A14527 and cat# A39240 respectively). HEK293T/17(cat# CRL-11268) and Vero E6 cells (cat# CRL-1586) were from ATCC.

METHOD DETAILS

Expression and purification of SARS-CoV-2 spike and RBD proteins

The mammalian expression vector that encodes the ectodomain of the SARS-CoV-2 S trimer was kindly provided by Jason McLellan (Wrapp et al., 2020). SARS-CoV-2 S trimer expression vector was transiently transfected into Expi293^{TM} cells using 1 mg/mL of polyethylenimine (Polysciences). Five days post transfection, the S trimer was purified using Strep-Tactin XT Resin (Zymo Research).

The SARS-CoV-2 RBD (residues 331-528), was cloned into the pVRC-8400 mammalian expression plasmid, with a C-terminal 6X-His-tag and an intervening HRV-3C protease cleavage site. Expression vector was transiently transfected into Human Embryonic Kidney (HEK) 293 GnTI- Freestyle cells suspension culture in serum-free media (Invitrogen) using polyethyleneimine (Polysciences). Media was harvested 4 days after transfection and the secreted protein purified using Ni-NTA IMAC Sepharose 6 Fast Flow resin (GE Healthcare) followed by size exclusion chromatography (SEC) on Superdex 200 (GE Healthcare) in 10 mM, Tris pH 8.0, 150 mM NaCl. Peak fractions containing RBD were pooled and HRV-3C protease (Thermo fisher, cat# SAE0045) was added in a mass ratio 1:100 relative to RBD, followed by incubation for 24 h at 20°C, to remove the C-terminal histidine-tag. The protein solution was again passed through the NI-NTA column to remove the His-tag and any traces of uncleaved protein. Protein purity was analyzed by SDS-PAGE and buffer exchanged to SEC buffer and concentrated to ~5 mg/mL and used for crystallization experiments.

Antibody production and mutagenesis

For each antibody, the variable genes were optimized for human cell expression and synthesized by GenScript. VH and VL were inserted separately into plasmids (gWiz or pcDNA3.4) that encoding the constant region for heavy chain and light chain respectively. Monoclonal antibodies were expressed in Expi293 (ThermoFisher, A14527) by co-transfecting heavy chain and light chain expressing plasmids using polyethylenimine (PEI, Linear, MV~25,000, Polysciences, Inc. Cat. No. 23966) and culture in 37.0C degree shaker at 125RPM and 8% CO2. Supernatants were collected on day 5, antibodies were purified by rProtein A Sepharose (GE, 17-1279-01) affinity chromatography.

For H4, the antibody expression constructs were synthesized (Gene Universal Inc, Newark DE) and subcloned into corresponding pVRC8400 vectors. To express the antibodies, equal among of heavy and light chain plasmid DNA were transfected into Expi293F cells (Life Technology) by using Turbo293 transfection reagent (Speed BioSystems). The transfected cells were cultured in shaker incubator at 120 rpm, 37°C, 9% CO2 for 5 days. Culture supernatants were harvested and purified over Protein A (GE Health Science) resin in columns. Each antibody was eluted with IgG elution buffer (Pierce), immediately neutralized with one tenth volume of 1M Tris-HCL pH 8.0. The antibodies were then buffer exchanged in PBS by dialysis.

Antibody gene mutations were introduced by QuikChange II site directed mutagenesis kit (Agilent, cat#200524)

Production of Fab from IgG

Fab fragments were produced from purified IgGs of monoclonal antibodies 2-15, 2-43 and H4 by digestion with Papain in the presence of the reducing agent 30 mM cysteine and were purified by affinity chromatography on protein A following the manufacturer's protocols (Thermo fisher). The purity of the resultant Fabs was analyzed by SDS-PAGE, and buffer exchanged into SEC buffer (10 mM Tris pH 7.4 and 150 mM NaCl) for crystallization experiments.

IgG Surface Plasmon Resonance binding experiments

SPR binding assays for IgGs binding to spike, were performed using a Biacore T200 biosensor, equipped with a Series S CM5 chip (cat# BR100030, Cytiva, MA), in a running buffer of 10mM HEPES pH 7.4, 150mM NaCl, 3 mM EDTA, 0.05% P-20 (HBS-EP+ buffer, Cytiva, MA) at 25°C. SARS-CoV-2 spike protein was captured through its C-terminal his-tag over an anti-his antibody surface. These surfaces were generated using the His-capture kit (Cat#: 28995056, Cytiva, MA) according to the instructions of the manufacturer, resulting in approximately 10,000 RU of anti-his antibody over each surface. Spike protein was captured over a single flow cell at a capture level of 125-200 RU. An anti-his antibody surface was used as a reference flow cell to remove bulk shift changes from the binding signal.

IgGs were tested using a three-fold dilution series of IgGs with concentrations ranging from 33.3 nM to 1.2 nM. The association and dissociation rates were each monitored for 55 s and 300 s respectively, at 50 μL/min. The bound spike/IgG complex was regenerated from the anti-his antibody surface using 10 mM Glycine pH 1.5. Blank buffer cycles were performed by injecting running buffer instead of IgG to remove systematic noise from the binding signal. The resulting data was processed and fit to a 1:1 binding model using Biacore Evaluation Software.

Pseudovirus neutralization assays

Recombinant Indiana VSV (rVSV) expressing SARS-CoV-2 spikes were generated as previously described (Han et al., 2021; Liu et al., 2020b). HEK293T cells were grown to 80% confluency before transfection with pCMV3-SARS-CoV-2-spike (kindly provided by Dr. Peihui Wang, Shandong University, China) using FuGENE 6 (Promega). Cells were cultured overnight at 37°C with 5% CO_2. The next day, medium was removed and VSV-G pseudo-typed ΔG-luciferase (G*ΔG-luciferase, Kerafast) was used to infect the cells in DMEM at an MOI of 3 for 1 hr before washing the cells with 1X DPBS three times. DMEM supplemented with anti-VSV-G antibody (I1, mouse hybridoma supernatant from CRL-2700; ATCC) was added to the infected cells and they were cultured overnight as described above. The next day, the supernatant was harvested and clarified by centrifugation at 300 g for 10 min and aliquots stored at −80°C.

Neutralization assays were performed by incubating pseudoviruses with serial dilutions of antibodies, and scored by the reduction in luciferase gene expression. In brief, Vero E6 cells were seeded in a 96-well plate at a concentration of 2×10^4 cells per well. Pseudoviruses were incubated the next day with serial dilutions of the test samples in triplicate for 30 mins at 37°C. The mixture was added to cultured cells and incubated for an additional 24 hr. The luminescence was measured by Britelite plus Reporter Gene Assay System (PerkinElmer). IC_{50} was defined as the dilution at which the relative light units were reduced by 50% compared with the virus control wells (virus + cells) after subtraction of the background in the control groups with cells only. The IC_{50} values were calculated using non-linear regression in GraphPad Prism.

Antibody gene assignments and genetic analyses

The 158 SARS-COV-2 neutralizing antibodies were collected from ten publications. We annotated these antibodies using IgBLAST-1.16.0 with the default parameters (Ye et al., 2013). For antibodies which have cDNA sequences deposited, the V and J genes were assigned using SONAR version 2.0 (https://github.com/scharch/sonar/) with germline gene database from IMGT (Lefranc et al., 2009; Schramm et al., 2016). For each antibody, the N-addition, D gene, and P-addition regions were annotated by IMGT V-QUEST (Brochet et al., 2008). To identify somatic hypermutations, each antibody sequence was aligned to the assigned germline gene using MUSCLE v3.8.31 (Edgar, 2004). Somatic hypermutations were identified from the alignment. In addition, the analysis of single cell antibody repertoire sequencing data of SARS-CoV-2 patient 2 from Liu et al. (2020b), from which 2-15 and 2-43 were isolated, showed that 29 of the 38 unique transcripts assigned to IGLV2-14*01 share nucleotide mutations G156T and T165G. These mutations lead to amino acid mutations E50D and N53K. Both nucleotide mutations are also observed in 82 of 90 unique IGLV2-14 transcripts from patient 1 of the same study. Because these transcripts having different VJ recombination and paired with different heavy chain genes, the chances that the two convergent mutations are the results of somatic hypermutation are very low. Thus, we suspect that both donors contain a new IGVL2-14 gene allele (IGVL2-14*0X), which was deposited to European Nucleotide Archive (ENA) with project accession numbers: PRJEB31020. 2-43 and 2-15 were assigned to the IGLV2-14*0X allele.

Cryo-EM data collection and processing

For mAb 2-43, SARS-CoV-2 spike protein at a concentration of 2 mg/ml was incubated with six-fold molar excess per spike trimer of the antibody Fab fragments for 30 minutes in 10 mM sodium acetate pH 5.5, 150 mM NaCl, and 0.005% n-dodecyl-β-D-maltoside (DDM). 2μL of the sample was incubated on C-flat 1.2/1.3 carbon grids for 30 s and vitrified using a Leica EM GP. Data were collected on a Titan Krios electron microscope operating at 300 kV, equipped with a Gatan K3 direct electron detector and energy filter, using the Leginon software package (Suloway et al., 2005). A total electron fluence of 51.69 e-/Å2 was fractionated over 40 frames, with a total exposure time of 2.0 s. A magnification of 81,000x resulted in a pixel size of 1.058 Å, and a defocus range of −0.4 to −3.5 μm was used.

For mAb 2-15, SARS-CoV-2 spike protein at a concentration of 1 mg/ml was incubated with a molar ratio of 1:1 Fab fragments to spike trimer for 30 minutes in 10 mM sodium acetate pH 5.5, 150 mM NaCl, and 0.005% % DDM. 2μL of the sample was incubated on C-flat 1.2/1.3 carbon grids for 30 s and vitrified using a Leica EM GP. Data were collected on a Titan Krios electron microscope operating at 300 kV, equipped with a Gatan K3 direct electron detector and energy filter, using the Leginon software package (Suloway et al., 2005). A total electron fluence of 52.40 e-/Å2 was fractionated over 60 frames, with a total exposure time of 3.0 s. A magnification of 81,000x resulted in a pixel size of 1.070 Å, and a defocus range of −0.8 to −3.4 μm was used.

For mAb H4, SARS-CoV-2 spike protein at a concentration of 1 mg/ml was incubated with eight-fold molar excess per spike trimer of the antibody Fab fragments for 30 minutes in 10 mM sodium acetate pH 5.5, 150 mM NaCl, and 0.005% % DDM. 2μL of the sample was incubated on C-flat 1.2/1.3 carbon grids for 30 s and vitrified using a Leica EM GP. Data were collected on a Titan Krios electron microscope operating at 300 kV, equipped with a Gatan K3 direct electron detector and energy filter, using the Leginon software package. A total electron fluence of 42.00 e-/Å2 was fractionated over 40 frames, with a total exposure time of 3.0 s. A magnification of 81,000x resulted in a pixel size of 1.070 Å, and a defocus range of −0.5 to −3.5 μm was used.

All processing was done using cryoSPARC v2.15.0 (Punjani et al., 2017). Raw movies were aligned and dose-weighted using patch motion correction, and the CTF was estimated using patch CTF estimation. A small subset of approximately 200 micrographs were picked using blob picker, followed by 2D classification and manual curation of particle picks, and used to train a Topaz neural network. This network was then used to pick particles from the remaining micrographs, which were extracted with a box size of 384 pixels.

For the mAb 2-43 dataset, 2D classification followed by *ab initio* modeling and 3D heterogeneous refinement revealed 61,434 particles with three Fabs bound, one to each RBD. A reconstruction of these particles with imposed C3 symmetry resulted in a 3.78 Å

map, as determined by gold standard Fourier shell correlation (FSC). Symmetry expansion followed by masked local refinement was used to obtain a 3.81 Å map of the Fab and RBD. The remainder of the S trimer was subjected to local refinement to obtain a 3.61 Å map. These two separate local refinements were aligned and combined using the vop maximum function in UCSF Chimera (Pettersen et al., 2004). This was repeated for the half maps, which were used along with the refinement mask from the global non-uniform refinement to calculate the 3D FSC (ref) and obtain an estimated resolution of 3.60 Å. All maps have been submitted to the EMDB with the ID EMDB-23165.

For the mAb 2-15 dataset, 2D classification followed by *ab initio* modeling and 3D heterogeneous refinement revealed 16,590 particles with one Fab bound to an RBD in the 'down' conformation and 21,456 particles with one Fab bound to an RBD in the 'up' conformation. The particles with Fab bound to RBD down were refined using Non-uniform refinement and C1 symmetry to a global resolution of 5.73 Å as determined by gold standard FSC. The RBD and Fab were masked and subjected to local refinement to obtain a map at 6.21 Å. The remainder of the trimer was also refined locally to 5.63 Å. A consensus map was obtained as described for mAb 2-43, with a resolution of 5.87 Å. All maps have been submitted to the EMDB with the ID EMDB-23166.

For the mAb H4 dataset, 2D classification followed by *ab initio* modeling and 3D heterogeneous refinement revealed 102,290 particles with one Fab bound to an RBD in the 'up' conformation. No classes with Fab bound to 'down' RBD were identified. 3D Variability Analysis was used to visualize the significant conformational heterogeneity of the 'up' RBD. Using the first and last frames of the reaction coordinate as reference maps, representing the extremes of the orientations adopted by the RBD, heterogeneous refinement was repeated to separate the Fab-bound spikes into more homogeneous classes. 56,080 particles adopted a more stable conformation and were refined to 4.78 Å using homogeneous refinement and C1 symmetry. Like the previously described datasets, the Fab and RBD were refined locally to 5.03 Å, with the remainder of the S trimer being refined to 4.32 Å. The final consensus map was estimated to have a resolution of 5.07 Å. All maps have been submitted to the EMDB with the ID EMDB-23167.

Cryo-EM model building

An initial homology model of the 2-43 Fab was built using Schrödinger Release 2020-2:BioLuminate (Zhu et al., 2014) and of H4 using ABodyBuilder (Leem et al., 2016). For mAb 2-15, the crystal structure determined here (PDB: 4HK0) was used as a starting model for the Fab variable domain and the associated RBD. For all models, the S trimer was modeled using the coordinates from PDB ID 6XEY. These models were docked into the consensus map using Chimera. The model was then fitted interactively using ISOLDE 1.0.1 (Croll, 2018) and COOT 0.8.9.2 (Emsley and Cowtan, 2004) and using real space refinement in Phenix 1.18 (Adams et al., 2004). For Fab 2-43, in cases were side chains were not visible in the experimental data, they were truncated to alanine except for residues very close to the RBD:Fab interface. Both H4 and 2-15 were built as poly-alanine models due to the low resolution of the experimental data. Validation was performed using Molprobity (Davis et al., 2004) and EMRinger (Barad et al., 2015). Models were submitted to the PDB with the following IDs: mAb 2-43 is 7L56, mAb H4 is 7L58, and 2-15 is 7L57. Figures were prepared using UCSF ChimeraX (Goddard et al., 2018).

X-ray data collection, structure solution, model building and refinement

For determination of the complex of with RBD, the two proteins were mixed at 1:1 molar ratio and incubated at 4.0°C for 60 min. RBD:2-15 complex was then isolated by gel filtration on Superdex-200 (GE Healthcare). Fractions containing complexes were pooled and concentrated to 6.5 mg/ml in SEC buffer. Screening for initial crystallization conditions was carried out in 96-well sitting drop plates using the vapor-diffusion method with a Mosquito crystallization robot (TTP LabTech) using various commercially available crystallization screens. Diffracting crystals were obtained from 0.1 M HEPES pH 7.5 and 70% MPD. Crystals were directly frozen and X-ray diffraction data was collected to 3.18 Å resolution at 100 K from a single flash-cooled crystal on beamline ID-C at the Advance Photon Source (APS) at Argonne National Laboratory. Diffraction data were processed with XDS (Kabsch, 2010) and scaled using AIMLESS (Evans, 2006) from the CCP4 software suite (Collaborative Computational ProjectNumber 4, 1994). Molecular replacement was performed with Phaser (McCoy et al., 2007), with previously reported RBD structure (PDB 7BZ5) and Fab (PDB code, 4HK0) as search models. Manual rebuilding of the structure using COOT (Emsley et al., 2010) was alternated with refinement using Phenix refine (Afonine et al., 2012) and PDB-REDO (Joosten et al., 2014). The Molprobity server was used for structure validation and PyMOL (version 2.1, Schrödinger, LLC) for structure visualization (Chen et al., 2010). A summary of the X-ray data collection and refinement statistics are shown in Table S2. PISA was used to identify paratope-epitope interfaces and to calculate buried surface area (Krissinel and Henrick, 2007). Hydrogen bonds were identified with a cutoff of 3.8Å. 2-15 model was submitted to the PDB with the following IDs: 7L5B.

Calculation of angle of approach

To measure the RBD approaching angle of antibodies, we first identify shared epitope residues among the five members of the VH1-2 antibody class. PyMOL was used to determine the center of mass of the shared epitope residues. We then determined the center of mass for heavy (the center of mass of the conserved Cys at 22 and 92) and light chains (the center of mass of the conserved Cys at 23 and 88). The heavy and light chain approaching angle was determined by linking the chain center of mass to the center of mass of the shared epitope. PyMOL was used to make structure figures. For antibody B38, the epitope center of mass was determined using the epitope residues of the antibody.

QUANTIFICATION AND STATISTICAL ANALYSIS

The statistical analyses for the pseudovirus neutralization assessments were performed using GraphPad Prism. The SPR data were fitted using Biacore Evaluation Software. Cryo-EM data were processed and analyzed using CryoSparc and Relion. Cryo-EM structural statistics were analyzed with Phenix and Molprobity. Statistical details of experiments are described in Method details or figure legends.

Cell Reports, Volume *35*

Supplemental information

Modular basis for potent SARS-CoV-2 neutralization by a prevalent VH1-2-derived antibody class

Micah Rapp, Yicheng Guo, Eswar R. Reddem, Jian Yu, Lihong Liu, Pengfei Wang, Gabriele Cerutti, Phinikoula Katsamba, Jude S. Bimela, Fabiana A. Bahna, Seetha M. Mannepalli, Baoshan Zhang, Peter D. Kwong, Yaoxing Huang, David D. Ho, Lawrence Shapiro, and Zizhang Sheng

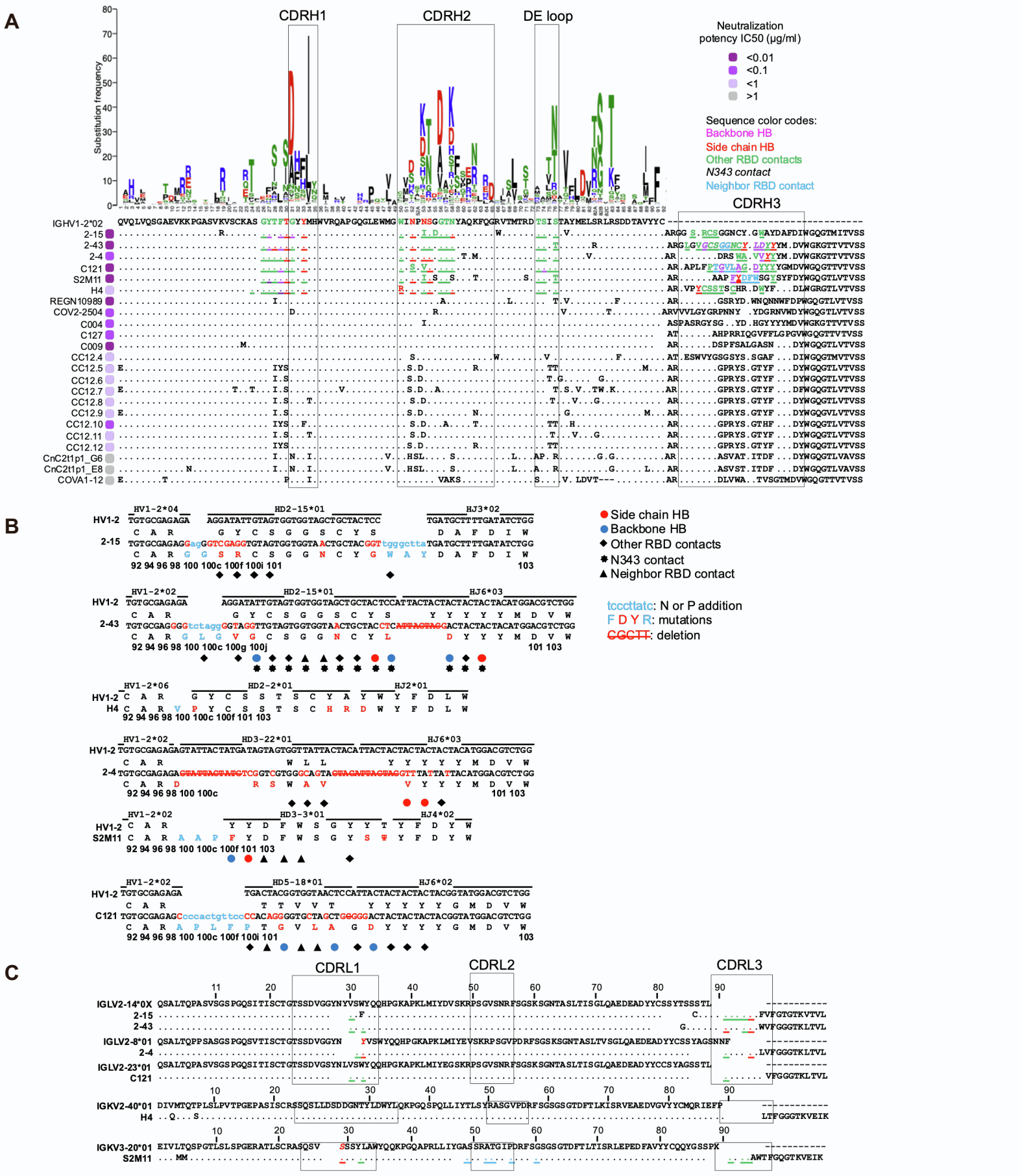

Figure S1. Alignment of heavy and light chain sequences of IGHV1-2 antibodies. Related to Figures 1, 3, 4, 5.

(A) Heavy chain sequence alignment of the VH1-2-derived antibodies with paratope residues of the VH1-2 class highlighted with underscore. Residues forming backbone hydrogen bonds, side chain hydrogen bond, hydrophobic contact with the SARS-CoV-2 RBD are colored magenta, red, green respectively. Residues contacting quaternary epitopes are colored cyan. Residues interacting with N343 glycan is shown with italic font. Antibody positions and CDR definitions are assigned using the Kabat scheme. The gene-specific substitution profile of VH1-2 gene shows the frequencies of somatic hypermutation to be generated by the somatic hypermutation machinery.

(B) Heavy chain gene recombination of the six VH1-2 antibodies. For H4 and S2M11, no N- or P-addition sites were determined because the nucleotide sequences are unavailable. H4 paratope residues were not identified due to low resolution of the structure.

(C) Light chain sequence alignment of the VH1-2 antibody class members with paratope residues highlighted with underscore.

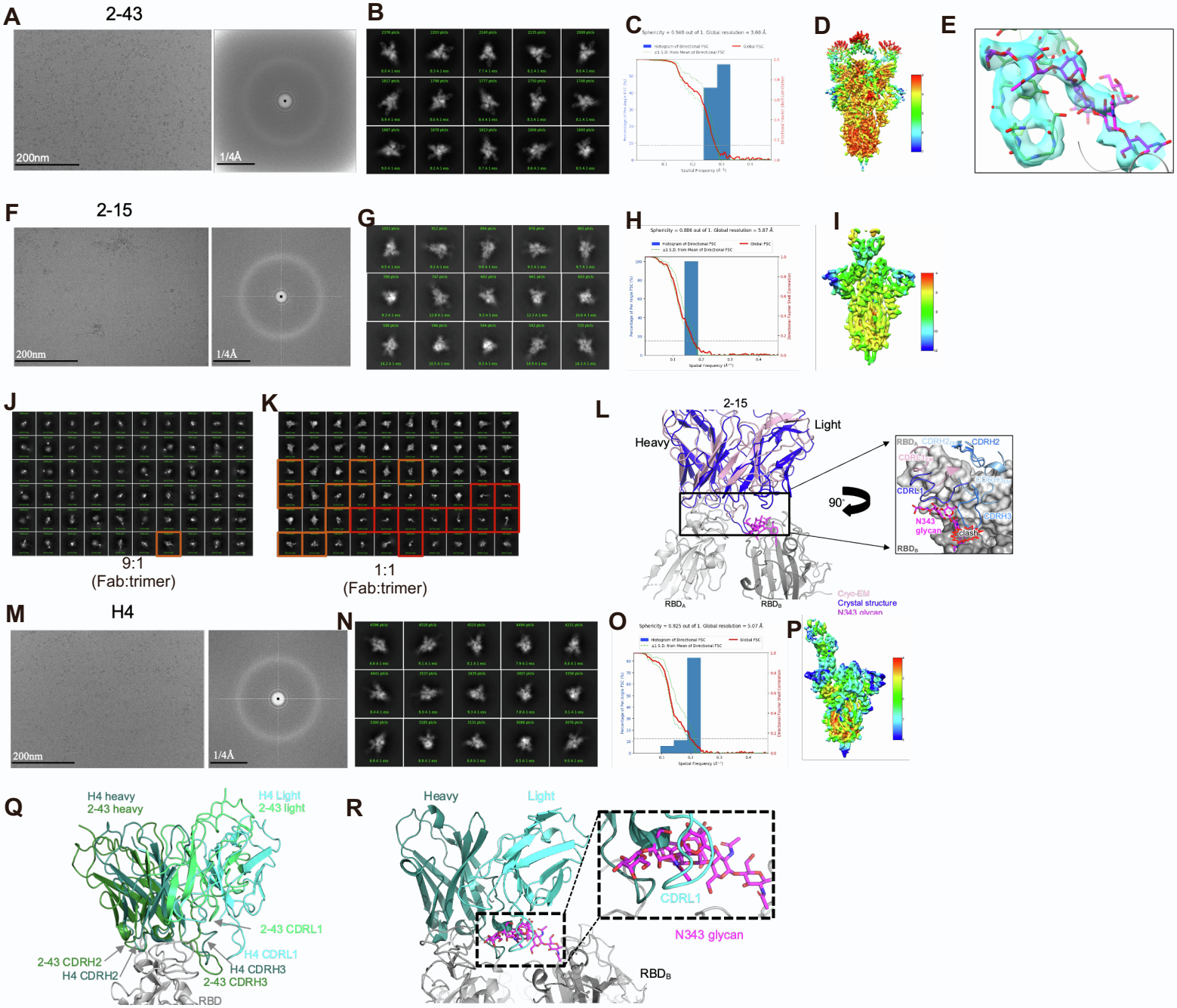

Figure S2. Cryo-EM data processing for antibody 2-43, 2-15, and H4 in complex with the S2P trimer. Related to Figures 2,3, and 4.

(A) Representative micrograph and CTF of the micrograph of 2-43 complexed with S trimer.
(B) Representative 2D class averages of 2-43/S complex.
(C) Resolution of the consensus map of 2-43 /S complex with C3 symmetry as calculated by 3DFSC.
(D) The local resolution of the full map of 2-43 as calculated by cryoSPARC at an FSC cutoff of 0.5. e, Representative density of the Fab 2-43 and RBD interface.
(E) Interaction of 2-43 CDRH3 with N343 glycan of an adjacent RBD.
(F) Representative 2-15 micrograph and CTF of the micrograph.
(G) Representative 2D class averages of 2-15 complexed with S trimer.
(H) Resolution of Fab 2-15 in complex with S2P trimer.
(I) The local resolution of the full 2-15 map as calculated by cryoSPARC at an FSC cutoff of 0.5.
(J) Disassembly of the SARS-CoV-2 spike by Fab 2-15 in a Fab:S trimer ratio of 9:1. Dimeric spike highlighted in orange, monomeric spike highlighted in red.
(K) Disassembly of the SARS-CoV-2 spike by Fab 2-15 in a Fab:S trimer ratio of 1:1. Dimeric spike highlighted in orange, monomeric spike highlighted in red.
(L) Superimposition of 2-15 crystal structure to the 2-15 cryo-EM structure.
(M) Representative micrograph and CTF of the micrograph of H4 complexed with S trimer.
(N) Representative H4 2D class averages.
(O) Resolution of Fab H4 in complex with S trimer.
(P) The local resolution of the full H4 map as calculated by cryoSPARC at an FSC cutoff of 0.5.
(Q) Superimposition of H4 to 2-43/spike complex. The heavy chain of the two antibodies have similar binding mode while the light chain of H4 rotated towards the interface between two RBDs.
(R) Superimposition of H4 to 2-43/spike complex showed that the long CDRL1 of H4 may clash with N343 glycan from an adjacent RBD.

A Buried accessible surface area

	2-43		2-15		H4		2-4		S2M11		C121	
	RBD_A	RBD_B	RBD_A	RBD_B	RBD_A	RBD_B	RBD_A	RBD_B	RBD_A	RBD_B	RBD_A	RBD_B
FWH1	130.5	0	175.51	0	ND	0	129.15	0	122.93	0	112.35	0
CDRH1	18.38	4.18	27.7	0	ND	0	34.52	0	18.04	0	30.96	0
CDRH2	185.45	0	218.53	0	ND	0	266.16	0	191.4	0	161.8	0
FWH3	83.86	0	95.54	0	ND	0	58.68	0	61.74	0	115.52	0
CDRH3	210.06	380.85	194.35	0	ND	0	275.91	44.32	209.02	329.02	259.69	101.23
CDRL1	59.25	51.27	45.62	0	ND	0	34.3	34.43	19.34	110.16	19.84	0
CDRL2	0	14.12	0	0	ND	0	0	0	0	78.13	0	0
CDRL3	68.99	0	64.23	0	ND	0	93.07	0	35	0	39.54	0
Total paratope	625.99	450.42	645.97	0	ND	0	762.64	78.75	534.54	517.31	627.35	101.23
Total epitope	812.92	548.57	810.44	0	ND	0	785.72	74.9	671.75	469.65	822.12	73.56
Total	1438.9	998.99	1456.4	0	ND	0	1548.4	153.65	1206.3	986.96	1449.5	174.79

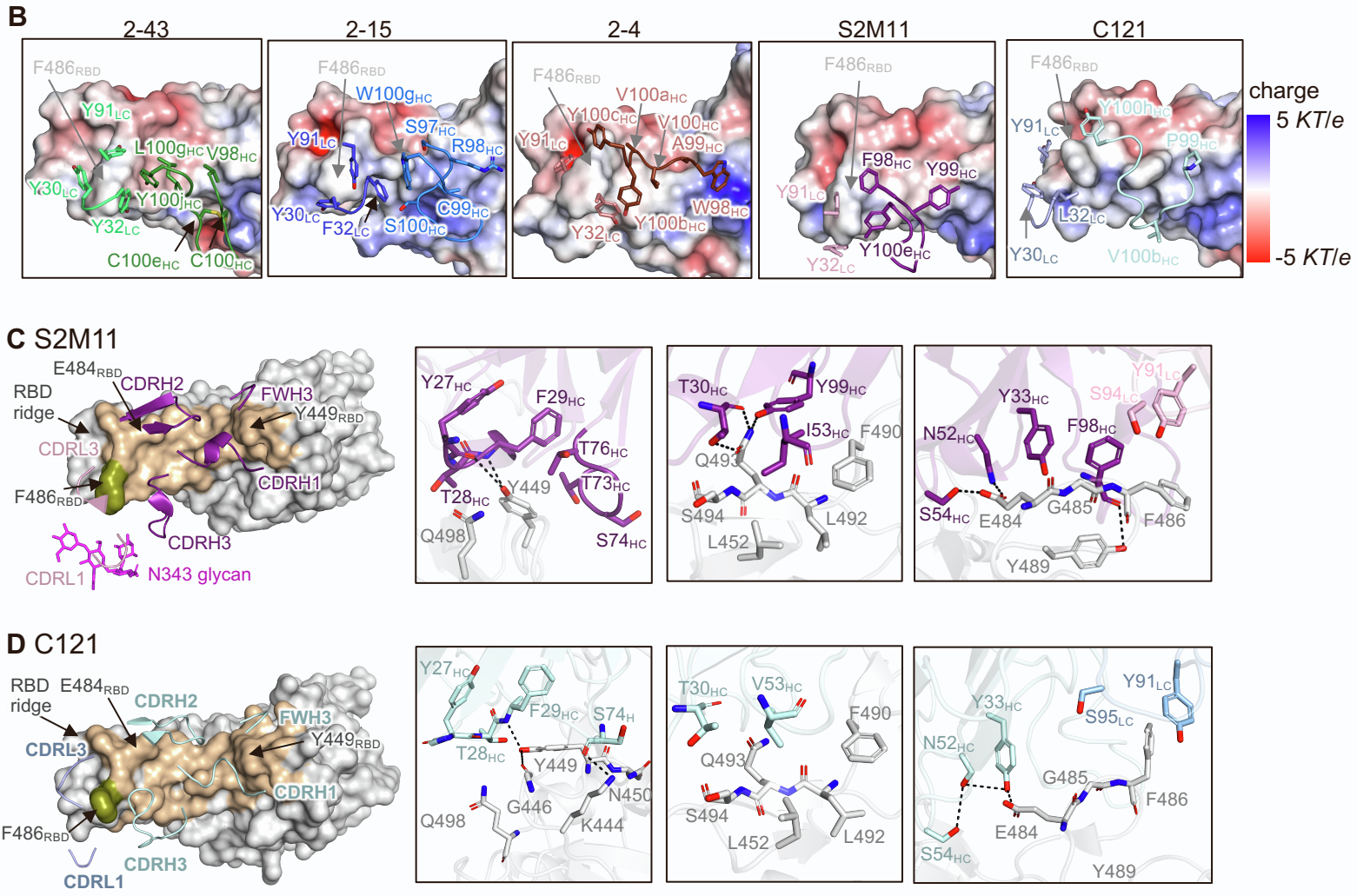

Figure S3. Paratope-epitope interactions of the VH1-2 antibody class. Related to figures 3, 4, 5, and 6.

(A) Buried accessible surface areas at paratope and epitope interfaces. Note: RBD_A is the RBD protomer with receptor binding motif recognized by antibody while RBD_B is the RBD protomer providing quaternary epitope.

(B) Hydrophobic interactions between antibody CDRH3, CDRL1, and CDRL3 and RBD. The RBD is colored with electrostatic potential. Side chains are shown for residues with buried accessible surface area more than 20Å^2.

(C) Overview of the S2M11 epitope (left panel) and close-up view of the hydrogen bond networks between S2M11 and the SARS-CoV-2 RBD (right three panels). The RBD epitope recognized by S2M11 heavy and light chains are colored wheat and orange respectively (RBD_A, light gray). Epitope residues interacting with both heavy and light chains were colored lemon. S2M11 also binds to N343 glycan (magenta) from a neighboring RBD (RBD_B, dark gray). Hydrogen bonds are shown as black dashed lines. PDB structure 7K43 is used.

(D) Overview of the C121 epitope (left panel) and close-up view of the hydrogen bond networks between C121 and the SARS-CoV-2 RBD (right three panels) (PDB ID 7K8X). The RBD epitope recognized by C121 heavy (palecyan) and light (lightblue) chains are colored wheat and orange respectively (RBD_A, light gray). Epitope residues interacting with both heavy and light chains are colored lemon.

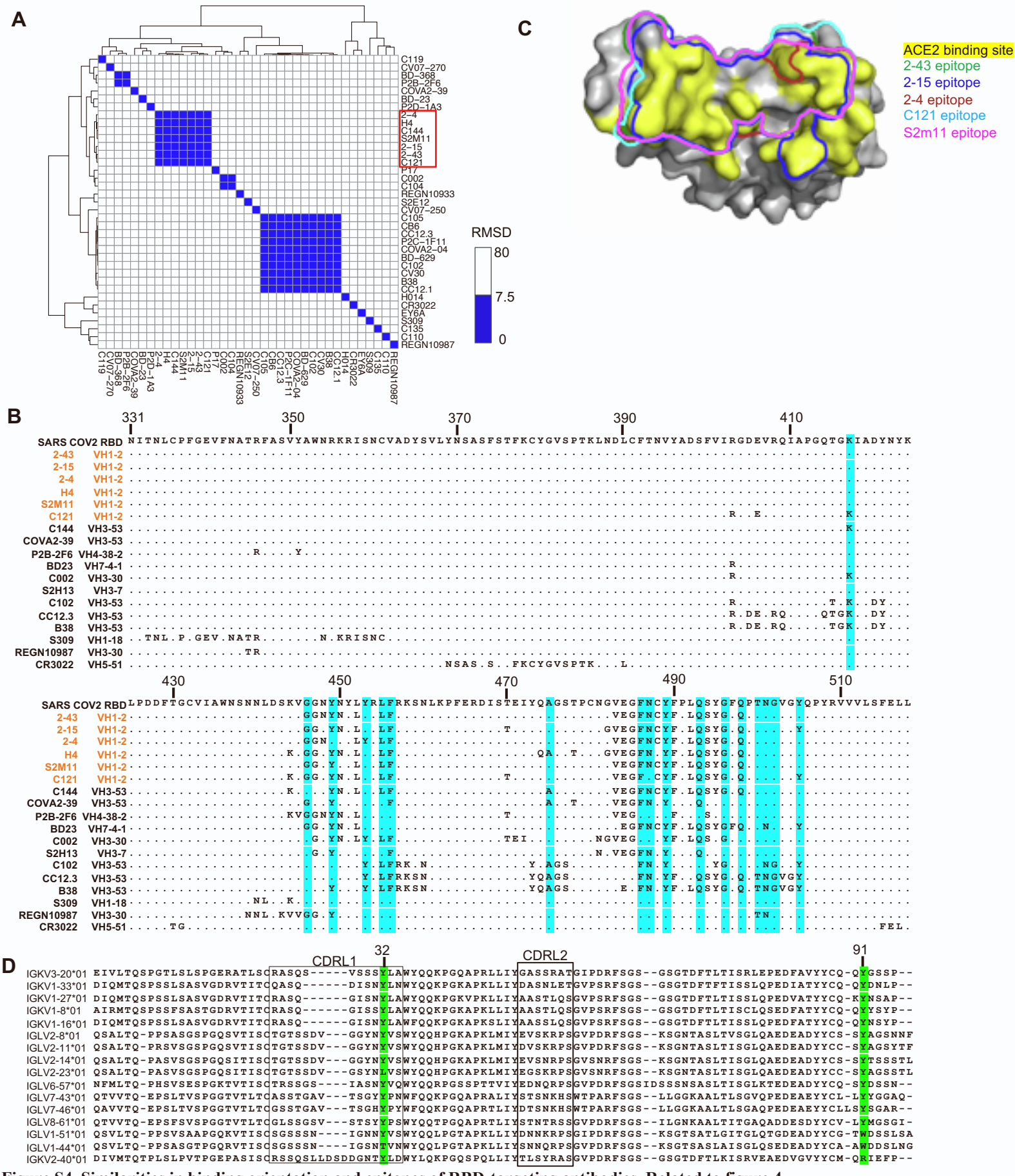

Figure S4. Similarities in binding orientation and epitopes of RBD-targeting antibodies. Related to figure 4.

(A) Clustering of SARS-CoV-2 RBD-targeting antibodies. For each pair of antibodies, the RBDs were superimposed and the RMSD of Ca atom between antibody variable domains were then calculated. Antibodies were then clustered using the calculated pairwise RMSD values.

(B) Epitope residues of SARS-CoV-2 RBD-targeting antibodies. For each antibody, epitope residues are shown and non-epitope residues are masked with dots. ACE2 binding site residues are highlighted with cyan background.

(C) The VH1-2 class antibodies have RBD epitopes that overlap with the ACE2 binding site.

(D) Alignment of the light chain germline genes used by the SARS-CoV-2 RBD-targeting VH1-2 antibodies in Figure 1C as well as other germline genes having residues $Y32_{LC}$ and $Y91_{LC}$.

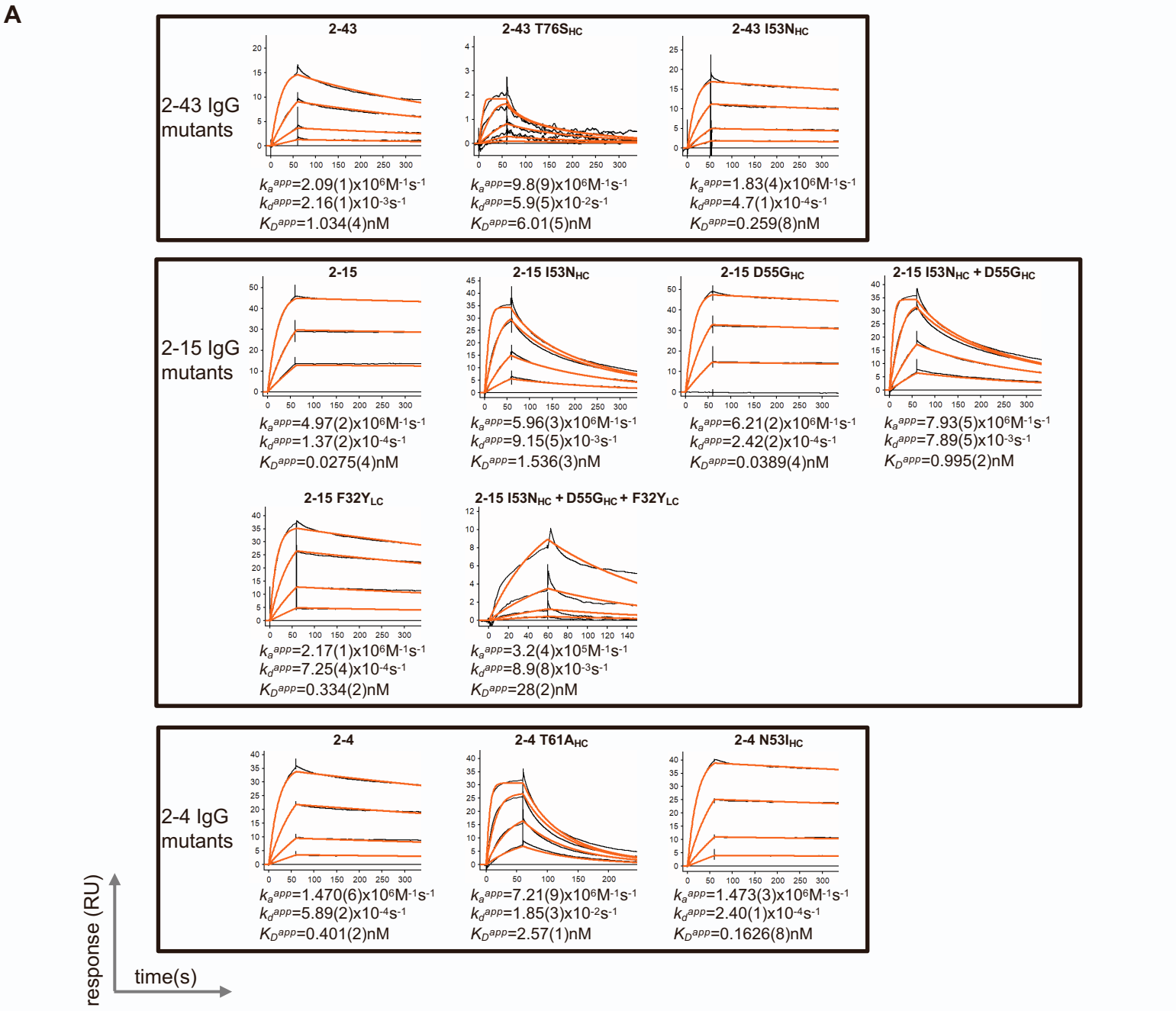

Figure S5. Apparent IgG binding affinity profiles, interaction of 53$_{HC}$ with RBD, and avidity effects of the VH1-2 antibodies. Related to figure 5.

(A) Surface plasmon resonance profiles of 2-43, 2-15, and 2-4 antibody variants. The black traces represent the experimental data, and the red traces represent the fit to an 1:1 Interaction model. The number in brackets represents the error of the fit in the last integer.

(B) Interaction of 53$_{HC}$ side chain with a hydrophobic pocket in RBD. RBD from 2-15/RBD complex is shown in surface mode and colored by electrostatic potential. APBS in PyMOL was used to calculate electrostatics.

(C) Pseudovirus neutralization profiles of Fabs 2-43, 2-15, and 2-4 showed significantly lower potency than IgG, suggesting avidity effect is important for achieving high neutralization potency. Data represent mean ± SEM of technical triplicates.

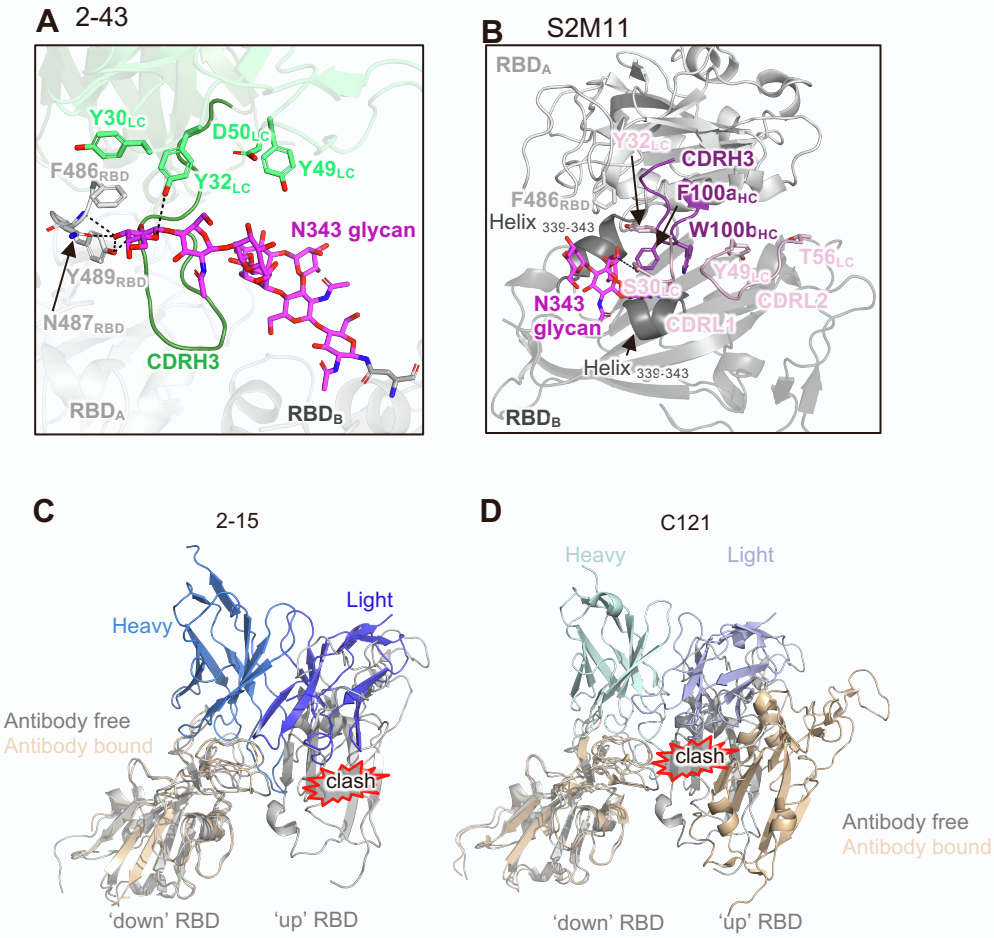

Figure S6. Quaternary recognition of 2-4 and S2M11 and potential interactions of 2-15, and C121 with adjacent 'up' RBDs. Related to Figure 6.

(A) The CDRL1 and CDRL2 (green) of 2-43 and RBD interact with one branch of the N343 glycan (magenta) from the adjacent RBD (RBD_B). The side chain of $D50_{LC}$ was modeled in PyMOL. N343 glycan also interacts with the RBD ridge in RBD_A.

(B) Close-up view of the S2M11 quaternary epitope between two RBDs mediated by CDRH3, CDRL1, and CDRL2.

(C) Superimposition of 2-15 in complex with RBD to antibody-free SARS-CoV-2 spike (PDBID: 6zgg). The light chain of 2-15 clashes with the adjacent 'up' RBD from the antibody free spike.

(D) Superimposition of C121 in complex with spike to antibody-free SARS-CoV-2 spike. The distance between the two RBD protomers increases in C121 bound spike, suggesting that the interaction of C121 light chain with the adjacent 'up' RBD induces conformation change in RBDs.

Table S1. SARS-CoV-2 neutralizing antibodies identified from infected humans. Related to Figure 1.

Antibody	IGHV	IGHJ	IGLV	IGLJ	Pseudovirus neutralization (IC_{50}, μg/mL)	live virus neutralization (IC_{50}, μg/mL)	Reference
1-20	IGHV3-53	IGHJ6	IGKV1-9	IGKJ3	0.127	0.008	Liu et al. 2020
1-57	IGHV3-72	IGHJ4	IGKV3-20	IGKJ2	0.009	0.008	Liu et al. 2020
1-68	IGHV1-24	IGHJ6	IGLV2-18*02	IGLJ1	0.767	0.014	Liu et al. 2020
1-87	IGHV1-24	IGHJ6	IGLV2-14	IGLJ1	0.095	0.086	Liu et al. 2020
2-15	IGHV1-2	IGHJ3	IGLV2-14	IGLJ1	0.005	0.001	Liu et al. 2020
2-17	IGHV1-69	IGHJ5	IGKV3-15	IGKJ4	0.168	0.007	Liu et al. 2020
2-30	IGHV3-30	IGHJ6	IGKV1-9	IGKJ4	0.512	0.050	Liu et al. 2020
2-36	IGHV4-61	IGHJ3	IGKV3-20	IGKJ1	0.044	0.209	Liu et al. 2020
2-38	IGHV3-21	IGHJ3	IGLV3-19	IGLJ3	0.232	0.208	Liu et al. 2020
2-4	IGHV1-2	IGHJ6	IGLV2-8	IGLJ3	0.394	0.057	Liu et al. 2020
2-43	IGHV1-2	IGHJ6	IGLV2-14	IGLJ3	0.071	0.003	Liu et al. 2020
2-51	IGHV1-24	IGHJ4	IGLV2-8	IGLJ3	0.652	0.007	Liu et al. 2020
2-7	IGHV2-5	IGHJ4	IGLV2-14	IGLJ3	0.010	0.003	Liu et al. 2020
4-18	IGHV3-30	IGHJ5	IGLV3-25	IGLJ3	0.023	0.020	Liu et al. 2020
4-19	IGHV4-59	IGHJ6	IGKV1-9	IGKJ4	0.070	0.109	Liu et al. 2020
4-20	IGHV1-46	IGHJ4	IGKV1-39	IGKJ1	0.036	0.017	Liu et al. 2020
4-8	IGHV1-69	IGHJ6	IGLV3-1	IGLJ3	0.032	0.009	Liu et al. 2020
5-24	IGHV3-33	IGHJ6	IGKV3-20	IGKJ4	0.013	0.008	Liu et al. 2020
5-7	IGHV1-46	IGHJ6	IGKV1-9	IGKJ3	0.050	0.033	Liu et al. 2020
B38	VH3-53/66	IGHJ6	IGKV1-9	IGKJ2	-	0.177	Wu et al., 2020
B5	VH1-2	IGHJ6	IGKV3-20	IGKJ1	-	1.375	Wu et al., 2020
H2	IGHV3-9	IGHJ5	IGKV1-39	IGKJ4	-	1.000	Wu et al., 2020
H4	VH1-2	IGHJ2	IGKV2-40	IGKJ2	-	0.896	Wu et al., 2020
C002	IGHV3-30	IGHJ4	IGKV1-39	IGKJ1	0.009	-	Robbiani et al., 2020
C003	IGHV3-53	IGHJ4	IGKV3-20	IGKJ2	0.314	-	Robbiani et al., 2020
C004	IGHV1-2	IGHJ6	IGKV1-33	IGKJ5	0.011	-	Robbiani et al., 2020
C005	IGHV1-58	IGHJ3	IGKV3-20	IGKJ1	0.060	-	Robbiani et al., 2020
C006	IGHV3-11	IGHJ6	IGLV1-44	IGLJ3	0.322	-	Robbiani et al., 2020
C008	IGHV3-30	IGHJ4	IGKV1-5	IGKJ1	0.625	-	Robbiani et al., 2020
C009	IGHV1-2	IGHJ4	IGLV2-8	IGLJ3	0.005	-	Robbiani et al., 2020
C013	IGHV1-69	IGHJ6	IGKV3-11	IGKJ4	0.042	-	Robbiani et al., 2020
C017	IGHV3-9	IGHJ5	IGKV3-11	NA	0.073	-	Robbiani et al., 2020
C022	IGHV4-39	IGHJ1	IGKV1-5	IGKJ2	0.074	-	Robbiani et al., 2020
C037	IGHV1-58	IGHJ3	IGKV3-20	IGKJ1	0.156	-	Robbiani et al., 2020
C101	IGHV3-53	IGHJ4	IGKV3-20	IGKJ1	0.008	-	Robbiani et al., 2020
C102	IGHV3-53	IGHJ4	IGKV3-20	IGKJ1	0.034	-	Robbiani et al., 2020
C103	IGHV4-34	IGHJ3	IGKV3-20	IGKJ4	0.004	-	Robbiani et al., 2020
C104	IGHV4-34	IGHJ3	IGKV3-20	IGKJ4	0.023	-	Robbiani et al., 2020
C105	IGHV3-53	IGHJ4	IGLV2-8	IGLJ3	0.026	-	Robbiani et al., 2020
C108	IGHV4-4	IGHJ3	IGLV2-14	IGLJ1	0.481	-	Robbiani et al., 2020
C110	IGHV5-51	IGHJ3	IGKV1-5	IGKJ2	0.018	-	Robbiani et al., 2020
C112	IGHV3-30	IGHJ4	IGLV2-14	IGLJ3	0.112	-	Robbiani et al., 2020
C115	IGHV3-49	IGHJ4	IGKV2-28	IGKJ2	0.198	-	Robbiani et al., 2020
C117	IGHV3-30	IGHJ4	IGLV1-51	IGLJ1	0.348	-	Robbiani et al., 2020
C118	IGHV3-30	IGHJ6	IGLV4-69	IGLJ3	0.104	-	Robbiani et al., 2020
C119	IGHV1-46	IGHJ6	IGLV2-14	IGLJ3	0.009	-	Robbiani et al., 2020
C120	IGHV3-53	IGHJ5	IGKV1-33	IGKJ4	0.013	-	Robbiani et al., 2020
C121	IGHV1-2	IGHJ6	IGLV2-23	IGLJ3	0.007	0.002	Robbiani et al., 2020
C122	IGHV3-53	IGHJ4	IGKV1-9	IGKJ2	0.023	-	Robbiani et al., 2020
C123	IGHV3-53	IGHJ3	IGKV1-9	IGKJ5	0.149	-	Robbiani et al., 2020
C124	IGHV3-48	IGHJ4	IGKV3-11	IGKJ1	0.342	-	Robbiani et al., 2020
C125	IGHV1-58	IGHJ3	IGKV3-20	IGKJ1	0.043	-	Robbiani et al., 2020

Table S1. Continued

C127	IGHV1-2	IGHJ6	IGLV1-44	IGLJ3	0.069	-	Robbiani et al., 2020
C128	IGHV3-23	IGHJ6	IGKV3-20	IGKJ4	0.101	-	Robbiani et al., 2020
C129	IGHV3-30	IGHJ3	IGKV1-33	IGKJ5	0.011	-	Robbiani et al., 2020
C131	IGHV1-69	IGHJ6	IGKV3-15	IGKJ5	0.031	-	Robbiani et al., 2020
C132	IGHV4-4	IGHJ4	IGLV2-14	IGLJ3	0.709	-	Robbiani et al., 2020
C135	IGHV3-30	IGHJ4	IGKV1-5	IGKJ1	0.017	0.003	Robbiani et al., 2020
C140	IGHV3-66	IGHJ6	IGKV1-9	IGKJ2	0.024	-	Robbiani et al., 2020
C144	IGHV3-53	IGHJ4	IGLV2-14	IGLJ1	0.007	0.003	Robbiani et al., 2020
C145	IGHV3-53	IGHJ4	IGLV2-14	IGLJ1	0.003	-	Robbiani et al., 2020
C149	IGHV3-30	IGHJ4	IGKV1-39	IGKJ4	0.045	-	Robbiani et al., 2020
C151	IGHV3-21	IGHJ5	IGLV6-57	IGLJ3	0.032	-	Robbiani et al., 2020
C152	IGHV1-18	IGHJ6	IGKV1-27	IGKJ1	0.022	-	Robbiani et al., 2020
C153	IGHV3-53	IGHJ4	IGLV2-23	IGLJ3	0.071	-	Robbiani et al., 2020
C154	IGHV3-30	IGHJ4	IGKV1-33	IGKJ5	0.436	-	Robbiani et al., 2020
C155	IGHV3-53	IGHJ4	IGKV3-15	IGKJ1	0.011	-	Robbiani et al., 2020
C161	IGHV4-34	IGHJ3	IGKV3-20	IGKJ4	0.042	-	Robbiani et al., 2020
C162	IGHV4-34	IGHJ3	IGKV3-20	IGKJ4	0.014	-	Robbiani et al., 2020
C163	IGHV4-34	IGHJ3	IGKV3-20	IGKJ4	0.010	-	Robbiani et al., 2020
C164	IGHV3-66	IGHJ3	IGLV2-23	IGLJ3	0.239	-	Robbiani et al., 2020
C165	IGHV1-69	IGHJ3	IGKV3-20	IGKJ1	0.041	-	Robbiani et al., 2020
C207	IGHV3-23	IGHJ4	IGKV3-11	IGKJ1	0.159	-	Robbiani et al., 2020
C210	IGHV3-53	IGHJ6	IGKV1-9	IGKJ4	0.051	-	Robbiani et al., 2020
C211	IGHV3-66	IGHJ4	IGKV3-15	IGKJ1	0.013	-	Robbiani et al., 2020
CC12.1	IGHV3-53	IGHJ6	IGKV1-9	IGKJ3	0.019	0.022	Rogers et al., 2020
CC12.10	IGHV1-2	IGHJ4	IGLV2-14	IGLJ3	0.070	0.058	Rogers et al., 2020
CC12.11	IGHV1-2	IGHJ4	IGLV2-14	IGLJ3	0.140	0.160	Rogers et al., 2020
CC12.12	IGHV1-2	IGHJ4	IGLV2-14	IGLJ3	1.500	0.540	Rogers et al., 2020
CC12.13	IGHV3-53	IGHJ4	IGKV1-33	IGKJ5	0.100	0.090	Rogers et al., 2020
CC12.14	IGHV3-21	IGHJ6	IGKV2-30	IGKJ3	0.023	0.089	Rogers et al., 2020
CC12.15	IGHV3-48	IGHJ4	IGLV1-40	IGLJ3	3.700	4.500	Rogers et al., 2020
CC12.16	IGHV3-33	IGHJ4	IGLV3-21	IGLJ3	>50	10.000	Rogers et al., 2020
CC12.17	IGHV3-30	IGHJ6	IGLV3-21	IGLJ3	2.100	8.600	Rogers et al., 2020
CC12.18	IGHV1-46	IGHJ4	IGLV6-57	IGLJ3	16.000	6.300	Rogers et al., 2020
CC12.19	IGHV3-23	IGHJ6	IGLV3-21	IGLJ3	>50	10.000	Rogers et al., 2020
CC12.2	IGHV3-53	IGHJ4	IGKV3-20	IGKJ2	0.220	0.016	Rogers et al., 2020
CC12.23	IGHV4-39	IGHJ4	IGLV3-25	IGLJ3	22.000	8.700	Rogers et al., 2020
CC12.3	IGHV3-53	IGHJ4	IGKV3-20	IGKJ2	0.018	0.026	Rogers et al., 2020
CC12.4	IGHV1-2	IGHJ3	IGLV2-8	IGLJ3	0.110	0.710	Rogers et al., 2020
CC12.5	IGHV1-2	IGHJ4	IGLV2-14	IGLJ3	0.330	0.520	Rogers et al., 2020
CC12.6	IGHV1-2	IGHJ4	IGLV2-14	IGLJ3	0.490	0.290	Rogers et al., 2020
CC12.7	IGHV1-2	IGHJ4	IGLV2-14	IGLJ3	0.260	0.460	Rogers et al., 2020
CC12.8	IGHV1-2	IGHJ4	IGLV2-14	IGLJ3	0.110	0.260	Rogers et al., 2020
CC12.9	IGHV1-2	IGHJ4	IGLV2-14	IGLJ3	23.000	0.610	Rogers et al., 2020
CC6.29	IGHV7-4-1	IGHJ5	IGKV1-39	IGKJ3	0.002	0.007	Rogers et al., 2020
CC6.31	IGHV1-46	IGHJ4	IGKV1-17	IGKJ4	0.059	0.053	Rogers et al., 2020
CC6.32	IGHV3-9	IGHJ4	IGLV3-21	IGLJ6	1.100	3.500	Rogers et al., 2020
COVA1-03	IGHV3-30	IGHJ6	IGKV1-27	IGKJ3	0.420	10.000	Brouwer et al., 2020
COVA1-12	IGHV1-2	IGHJ6	IGLV2-8	IGLJ3	1.300	1.400	Brouwer et al., 2020
COVA1-16	IGHV1-46	IGHJ1	IGKV1-33	IGKJ4	0.130	0.750	Brouwer et al., 2020
COVA1-18	IGHV3-66	IGHJ4	IGLV7-46	IGLJ3	0.008	0.007	Brouwer et al., 2020
COVA1-21	IGHV3-30	IGHJ6	IGKV3-15	IGKJ2	0.040	0.160	Brouwer et al., 2020
COVA1-22	IGHV1-18	IGHJ6	IGLV3-1	IGLJ3	0.180	10.000	Brouwer et al., 2020
COVA1-25	IGHV4-39	IGHJ6	IGKV1-5	IGKJ3	0.180	10.000	Brouwer et al., 2020
COVA2-02	IGHV4-39	IGHJ6	IGKV1-39	IGKJ3	3.100	10.000	Brouwer et al., 2020

Table S1. Continued

COVA2-04	IGHV3-53	IGHJ6	IGKV3-20	IGKJ3	0.220	2.500	Brouwer et al., 2020
COVA2-05	IGHV5-51	IGHJ6	IGKV1-33	IGKJ4	5.700	10.000	Brouwer et al., 2020
COVA2-07	IGHV3-53	IGHJ6	IGKV3-20	IGKJ3	0.029	0.025	Brouwer et al., 2020
COVA2-11	IGHV1-69	IGHJ4	IGKV3-20	IGKJ4	3.700	10.000	Brouwer et al., 2020
COVA2-13	IGHV3-53	IGHJ6	IGKV3-20	IGKJ1	3.200	9.900	Brouwer et al., 2020
COVA2-15	IGHV3-23	IGHJ4	IGKV2-30	IGKJ2	0.008	0.009	Brouwer et al., 2020
COVA2-17	IGHV1-69	IGHJ4	IGKV3-11	IGKJ1	0.053	10.000	Brouwer et al., 2020
COVA2-20	IGHV3-53	IGHJ6	IGKV1-17	IGKJ1	0.730	1.500	Brouwer et al., 2020
COVA2-29	IGHV3-30	IGHJ3	IGKV1-39	IGKJ1	0.092	0.130	Brouwer et al., 2020
COVA2-37	IGHV1-24	IGHJ5	IGLV1-40	IGLJ3	4.000	10.000	Brouwer et al., 2020
COVA2-39	IGHV3-53	IGHJ3	IGLV2-23	IGLJ3	0.036	0.054	Brouwer et al., 2020
P2A-1A10	IGVH1-2	n.d.	IGKV2-40	n.d.	-	1.640	Ju et al., 2020
P2A-1A8	IGHV3-9	n.d.	IGLV2-14	n.d.	-	10.000	Ju et al., 2020
P2B-2F6	IGHV4-38-2	IGHJ3	IGLV2-8	IGLJ3	-	0.410	Ju et al., 2020
P2B-2G4	IGHV3-33	n.d.	IGLV2-11	n.d.	-	2.900	Ju et al., 2020
P2C-1A3	IGHV3-11	n.d.	IGKV1-9	n.d.	-	0.280	Ju et al., 2020
P2C-1C10	IGHV1-69	n.d.	IGKV3-11	n.d.	-	10.000	Ju et al., 2020
P2C-1F11	VH3-66	n.d.	IGKV3-20	n.d.	0.030	0.030	Ju et al., 2020
cov2-2130	IGHV3-15	IGHJ4	IGKV4-1	IGKJ4	-	0.186	Zost et al., 2020
cov2-2355	IGHV1-58	IGHJ3	IGKV3-20	IGKJ1	-	0.019	Zost et al., 2020
cov2-2504	IGHV1-2	IGHJ4	IGLV1-44	IGLJ2	-	0.015	Zost et al., 2020
cov2-2514	IGHV3-20	IGHJ3	IGLV3-19	IGLJ2	-	0.463	Zost et al., 2020
cov2-2678	IGHV3-20	IGHJ3	IGLV3-19	IGLJ3	-	0.264	Zost et al., 2020
cov2-2838	IGHV1-58	IGHJ3	IGKV3-20	IGKJ1	-	0.107	Zost et al., 2020
cov2-2952	IGHV3-66	IGHJ6	IGKV1-9	IGKJ5	-	0.363	Zost et al., 2020
CnC2t1p1_B10	IGHV1-69	IGHJ4	IGKV3-11	IGKJ4	-	10.000	Kreer et al., 2020
CnC2t1p1_B4	IGHV1-18	IGHJ5	IGLV2-23	IGLJ3	-	0.780	Kreer et al., 2020
CnC2t1p1_D6	IGHV3-49	IGHJ6	IGKV2-28	IGKJ3	-	3.720	Kreer et al., 2020
CnC2t1p1_E12	IGHV3-49	IGHJ6	IGKV2-28	IGKJ3	-	3.130	Kreer et al., 2020
CnC2t1p1_E8	IGHV1-2	IGHJ4	IGLV2-23	IGLJ3	-	4.420	Kreer et al., 2020
CnC2t1p1_G6	IGHV1-2	IGHJ4	IGLV2-23	IGLJ3	-	10.000	Kreer et al., 2020
FnC1t1p2_A5	IGHV1-8	IGHJ4	IGKV3-20	IGKJ1	-	10.000	Kreer et al., 2020
FnC1t2p1_D4	IGHV7-4-1	IGHJ5	IGKV1-33	IGKJ4	-	0.280	Kreer et al., 2020
FnC1t2p1_G5	IGHV7-4-1	IGHJ5	IGKV1-33	IGKJ4	-	0.330	Kreer et al., 2020
HbnC2t1p2_D9	IGHV3-33	IGHJ6	IGKV3-11	IGKJ1	-	0.930	Kreer et al., 2020
HbnC3t1p1_C6	IGHV1-58	IGHJ3	IGKV3-20	IGKJ1	-	0.040	Kreer et al., 2020
HbnC3t1p1_F4	IGHV3-30	IGHJ5	IGKV1-5	IGKJ4	-	0.780	Kreer et al., 2020
HbnC3t1p1_G4	IGHV3-66	IGHJ4	IGKV3-20	IGKJ1	-	0.120	Kreer et al., 2020
HbnC3t1p2_B10	IGHV3-66	IGHJ4	IGKV3-20	IGKJ2	-	0.250	Kreer et al., 2020
HbnC3t1p2_C6	IGHV1-58	IGHJ3	IGKV3-20	IGKJ1	-	0.330	Kreer et al., 2020
HbnC4t1p1_D5	IGHV3-9	IGHJ4	IGKV1-39	IGKJ4	-	10.000	Kreer et al., 2020
REGN10933	IGHV3-11	IGHJ4	IGKV1-33	IGKJ4	0.043	0.043	Hansen et al., 2020
REGN10934	IGHV3-15	IGHJ2	IGKV1-33	IGKJ1	0.054	0.054	Hansen et al., 2020
REGN10954	IGHV3-66	IGHJ4	IGKV1-33	IGKJ1	0.092	0.092	Hansen et al., 2020
REGN10964	IGHV4-4	IGHJ4	IGKV1-39	IGKJ3	0.057	0.057	Hansen et al., 2020
REGN10977	IGHV1-69	IGHJ4	IGKV3-20	IGKJ1	0.052	0.052	Hansen et al., 2020
REGN10984	IGHV3-66	IGHJ6	IGLV1-51	IGLJ3	0.097	0.097	Hansen et al., 2020
REGN10986	IGHV3-66	IGHJ4	IGLV1-40	IGLJ1	0.099	0.099	Hansen et al., 2020
REGN10987	IGHV3-30	IGHJ4	IGLV2-14	IGLJ3	0.041	0.041	Hansen et al., 2020
REGN10989	IGHV1-2	IGHJ5	IGLV2-14	IGLJ3	0.007	0.007	Hansen et al., 2020
S2M11	IGVH1-2	IGHJ4	IGKV3-20	IGKJ1	0.002	0.001	Tortorici et al. 2020
S2E12	IGVH1-58	IGHJ3	IGKV3-20	IGKJ1	0.002	0.004	Tortorici et al. 2020

Table S2. Cryo-EM data collection, refinement and validation statistics. Related to Figure 2.

	SARS-CoV-2 spike with Fab 2-43 (EMDB-23165) (PDB 7L56)	SARS-CoV-2 spike with Fab H4 (EMDB-23167) (PDB 7L58)	SARS-CoV-2 spike with Fab 2-15 (EMDB-23166) (PDB 7L57)
Data collection and processing			
Magnification	81,000	81,000	81,000
Voltage (kV)	300	300	300
Electron exposure (e–/Å^2)	51.69	42.00	52.40
Defocus range (μm)	-0.4 to -3.5	-0.5 to -3.5	-0.8 to -3.4
Pixel size (Å)	1.058	1.070	1.070
Symmetry imposed	C3	C1	C1
Initial particle images (no.)	199,753	1,070,123	882,010
Final particle images (no.)	61,434	102,290	16,590
Map resolution (Å)	3.60	5.07	5.87
FSC threshold	0.143	0.143	0.143
Refinement			
Initial model used (PDB code)	6XEY	6XEY	#### for xtal structure 6XEY
Map-to-model resolution (Å)	3.8	4.7	6.4
FSC threshold	0.5	0.5	0.5
Map sharpening *B* factor (Å^2)	-110.3	-121.2	-209.3
Model composition			
Non-hydrogen atoms	26,583	18103	17,415
Protein residues	3686	3442	3192
Ligands	67	41	54
B factors (Å^2)			
Protein	77.79	142.43	232.59
Ligand	88.22	50.00	264.74
R.m.s. deviations			
Bond lengths (Å)	0.010	0.008	0.008
Bond angles (°)	1.094	1.340	1.287
Validation			
MolProbity score	1.27	1.57	1.73
Clashscore	0.98	1.89	2.57
Poor rotamers (%)	0.0	1.33	1.68
Ramachandran plot			
Favored (%)	92.14	90.74	91.22
Allowed (%)	7.86	8.99	8.62
Disallowed (%)	0.0	0.26	0.16

Table S3. Crystal structure data collection, refinement and validation statistics. Related to Figure 2.

	SARS-CoV-2 RBD in complex with 2-15 Fab
PDB ID	7L5B
Data Collection	
Space group	I 1 2 1
Unit cell dimensions	
a,b,c (Å)	134.013 70.439 140.039
α,β,γ (°)	90 96.932 90
Resolution range (Å)	102.49 - 3.182 (3.295 - 3.182)*
Total reflections	37768 (7212)
Unique reflections	20304 (2877)
Completeness (%)	93.26 (70.8)
Redundancy	2.7 (2.5)
$I/\sigma(I)$	12.80 (1.8)
R_{merge}	0.051 (0.630)
$CC_{1/2}$	0.989 (0.437)
Refinement	
Resolution range (Å)	102.49 - 3.182
Number of complexes per asymmetric unit	1
R_{work}/R_{free}	19.1/23.8
Number of atoms	
Protein	599
Ligands	0.0
B-factors	
Protein	64.10
RMS deviations	
Bond lengths (Å)	0.010
Bond angles (°)	1.41
Ramachandran statistics	
Favored (%)	86.37
Allowed (%)	13.63
Outliers (%)	0